

# Acoustic metamaterials

EP

Cite as: J. Appl. Phys. 129, 171103 (2021); doi: 10.1063/5.0046878

Submitted: 8 February 2021 · Accepted: 12 April 2021 ·

Published Online: 5 May 2021



View Online



Export Citation



CrossMark

Jensen Li,<sup>a)</sup> Xinhua Wen, and Ping Sheng<sup>b)</sup>

## AFFILIATIONS

Department of Physics, HKUST, Clear Water Bay, Kowloon, Hong Kong, China

<sup>a)</sup>Email: [jensenli@ust.hk](mailto:jensenli@ust.hk)<sup>b)</sup>Author to whom correspondence should be addressed: [sheng@ust.hk](mailto:sheng@ust.hk)

## ABSTRACT

Waves are generally characterized by angular frequency  $\omega$  and wavevector  $\mathbf{k}$ . Accordingly, this tutorial is structured into two parts, one on resonance-based acoustic metamaterials, in the frequency domain, and one on topological acoustics, based on the wavevector domain as topological structures inherently involve spatial configurations that are a step beyond the simple periodic lattices. Each part will begin with a brief introduction of the basic principles, followed by two examples described in detail. In the first part, we present decorated membrane resonators and the broadband optimal acoustic absorption structures, the latter being crucial for the potential applications of acoustic metamaterials. In the second part, we discuss how to construct the Dirac cone, a special type of dispersion from either accidental degeneracy or symmetry protection, which can be shown to lead to negative, zero, or positive refractive indices. The shifting and gapping of these Dirac cones in the reciprocal space can result in effects on acoustic waves similar to that of a magnetic field on an electron. More generally, they lead to edge states resulting from a real-space gauge field as well as topological bandgaps.

Published under an exclusive license by AIP Publishing. <https://doi.org/10.1063/5.0046878>

## I. INTRODUCTION

Acoustic waves in air satisfy the scalar wave equation

$$\frac{1}{v^2} \frac{\partial^2 p(t, \mathbf{x})}{\partial t^2} - \nabla^2 p(t, \mathbf{x}) = 0, \quad (1)$$

where  $v$  denotes the wave speed, which has the value  $v_0 = \sqrt{\gamma P_0 / \rho_0} = 340 \text{ m/s}$  in air, where  $P_0 = 1.01 \times 10^5 \text{ Pa}$  is the atmospheric pressure,  $\rho_0 = 1.21 \text{ kg/m}^3$  is the air density, and  $\gamma = 1.4$  is the adiabatic index of air. In Eq. (1),  $p = P - P_0$  represents the pressure modulation of sound, where  $P$  is the instantaneous pressure. Solution to Eq. (1) has the general functional form  $p(\omega t \pm \mathbf{k} \cdot \mathbf{x})$  with the dispersion relation

$$|\mathbf{k}|^2 = k^2 = \frac{\omega^2}{v^2}, \quad (2)$$

as can be easily verified through differentiation. Among all the possible wave functional forms, the plane wave  $\exp[-i(\omega t \pm \mathbf{k} \cdot \mathbf{x})]$  is the most common. To supplement Eqs. (1) and (2), we also have Newton's law that relates the pressure modulation and displacement (particle) velocity  $\mathbf{u} = \partial \xi / \partial t$ , where  $\xi$  denotes the air displacement of the sound wave,

$$-\nabla p = \rho_0 \frac{\partial \mathbf{u}}{\partial t}, \quad (3)$$

and the continuity equation

$$\frac{\partial \rho}{\partial t} + \rho_0 \nabla \cdot \mathbf{u} = 0, \quad (4)$$

where  $\rho$  denotes the instantaneous density. In what follows, we will treat those cases in which the metamaterial sample has a planar interface with air. Hence, we will regard both the displacement and displacement velocity as complex scalar quantities,  $\xi$  and  $\mathbf{u}$ , that represent the components of the two vectors normal to the interface.

The  $\omega$  and  $\mathbf{k}$  characterization of the acoustic waves foreshadows the development of acoustic metamaterials, initially in the realm of resonance-based structures that can display sample characteristics such as the subwavelength sample size, together with their wave manipulation characteristics not found in naturally occurring materials. More recently, the advent of topological quantum phenomena has propelled a new direction based on novel spatial structures, i.e., in the wavevector domain, that have topological features distinct from the periodic structures. This tutorial is accordingly divided into two sections, each with two examples. For the

resonance-based acoustic metamaterials,<sup>1–17</sup> membrane-type acoustic metamaterials will be used as the first example since it involves several general concepts that can be applied in many other contexts. The second example is the optimal acoustic absorption structure, which can display tunable absorption spectrum over arbitrarily broad frequency band and thereby eliminates one of the major drawbacks of metamaterials for potential applications. For the second part, we will discuss phononic crystals in the diffraction regime, which can be utilized to make special types of dispersions, such as negative and zero indices as the first example. It is related to Dirac cone dispersion from an accidental degeneracy. In the second example, we will move to another type of Dirac cone dispersion enabled by symmetry protection—by lowering spatial or lattice symmetries to induce gauge field or topological bandgap in which quantum-Hall-like edge states or topological one-way edge states can be realized and observed. These principles do not rely on resonance and are generic to both acoustic and elastic waves in solid. Rather than trying to cover a broad swath of this growing field, our intention here is to use examples to elucidate the basic concepts underlying the acoustic metamaterials, hopefully to lay the groundwork for the readers to further explore this rapidly evolving area.

## II. RESONANCE-BASED METAMATERIALS

Resonance-based metamaterials can manipulate waves with subwavelength sample sizes, in contrast to phononic crystals whose wave characteristics are only apparent when sample's structural periodicity is comparable to the relevant wavelength. In this section, we detail two examples with emphasis on explaining the relevant concepts together with the pertinent mathematics involved.

### A. Preliminaries

In an acoustically resonant system with resonance frequency  $\Omega$ , the magnitude of displacement response  $\xi(\omega)$  of the system to a pressure modulation  $p(\omega)$  has the general form

$$\xi = \frac{p(A/m)}{\Omega^2 - \omega^2 - i\beta\omega}, \quad (5)$$

where  $p$  is the actual pressure on the sample that includes the pressure from both the incident and reflected waves,  $A$  and  $m$  denote the relevant area and inertial mass of the resonator, respectively, and  $\beta$  is a dissipation coefficient in units of frequency. The Green function is defined as

$$G = \frac{\xi}{p} = \frac{A}{m} \left( \frac{1}{\Omega^2 - \omega^2 - i\beta\omega} \right). \quad (6)$$

The quantity in the bracket has the functional form denoted as a “Lorentzian,” which characterizes almost all the resonances. In acoustics, an important parameter is the impedance,

$$Z = \frac{p}{u} = \frac{p}{-i\omega\xi} = \frac{1}{-i\omega G}. \quad (7)$$

For a plane wave in air,  $Z_0 = \rho_0 v_0$ . The real part of the Green function is non-dissipative; its dissipative imaginary part corresponds to the real part of impedance. Equation (7) is generally true for samples with subwavelength lateral dimensions so that diffraction is not a concern. The inverse relationship between the Green function and impedance is especially convenient for evaluating the impedance of resonance-based metamaterials since the Green function can always be written as the sum of Lorentzians for resonators with different resonance frequencies, which can always be obtained, in conjunction with the eigenfunction configurations, either analytically or through numerical simulations for resonators with complex geometries.

We note here some special properties of the Lorentzian that can be useful for later developments. In the limit of vanishing  $\beta$ , we have

$$\lim_{\beta \rightarrow 0} \left( \frac{1}{\Omega^2 - \omega^2 - i\beta\omega} \right) = P \frac{1}{\Omega^2 - \omega^2} + i \frac{\pi}{2\omega} \delta(\Omega - \omega), \quad (8)$$

where  $P$  denotes taking the principal value of the quantity that follows. It might appear puzzling why there can be an imaginary part, which represents dissipation, even when the dissipation coefficient  $\beta$  is zero. The reason is that as  $\beta$  diminishes, the resonance peak becomes sharper, implying an increasing  $Q$  factor of the resonator. As  $Q$  approaches infinity, the lifetime of the resonance also approaches infinity; hence even with an infinitesimal dissipation coefficient there can be finite dissipation over an infinite duration. This is the meaning of the delta function imaginary part, which can also be regarded as the density of resonant mode per unit frequency, localized at  $\Omega$ .

### B. Decorated membrane resonator

A decorated membrane resonator (DMR) consists of a thin polymeric membrane, such as Latex, slightly stretched over a fixed boundary with one or multiple pieces of solid weight glued on top.<sup>6</sup> The solid piece(s) can be in different shapes. Here, we consider the simplest case of a circular membrane with a circular weight in the center. Such a resonator can have multiple resonances; here we will be concerned with only the two lowest frequency resonance eigenmodes whose profiles,  $\xi_{1(2)}(x_{||})$ , are depicted schematically in Fig. 1. Here,  $x_{||}$  denotes the coordinate in the plane of the membrane, whereas the displacement  $\xi$  is normal to the plane as noted earlier and generally much smaller than the wavelength. The resonance frequencies of the DMR can be especially low, because the restoring force of the membrane is weak. Hence, the relevant wavelength can be order(s) of magnitude larger than the size of the DMR.

A resonator can be classified to have a dipolar symmetry if its resonance involves center of mass motion. DMR is a dipolar resonator. In contrast, Helmholtz resonator<sup>5</sup> is monopolar in symmetry since at its resonances involves no center of mass movement.

#### 1. Anti-resonance and the effective dynamic mass density

If we denote  $\Omega_1$  and  $\Omega_2$  as the two lowest resonance frequencies of a DMR, then the sample area-averaged displacement response can be written as

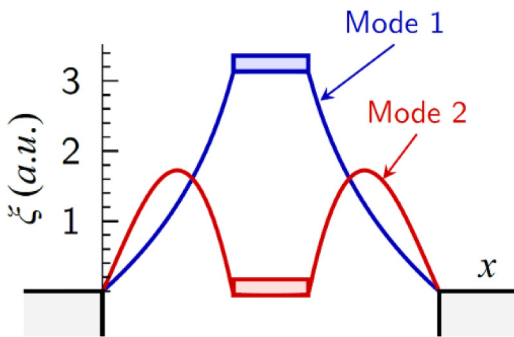


**FIG. 1.** A schematic illustration of the lowest frequency eigenmode, in blue color, and the second lowest frequency eigenmode, in red color, for the decorated membrane resonator (DMR). The rectangle indicates the solid platelet. Here  $x$  denotes the coordinate axis in middle of the DMR's plane, and  $\xi_{1,2}$  denotes the displacement normal to the plane for the two eigenmodes. Adapted from Ref. 13.

$$\langle \xi(\omega) \rangle = \frac{\alpha_1}{\Omega_1^2 - \omega^2 - i\beta_1\omega} + \frac{\alpha_2}{\Omega_2^2 - \omega^2 - i\beta_2\omega} \quad (9)$$

by neglecting the higher order resonant modes. Here,  $\alpha_{1,2}$  are positive constants and the angular brackets  $\langle \rangle$  denote area averaging. For an incident acoustic wave with frequency  $\omega$  that is intermediate between  $\Omega_1$  and  $\Omega_2$  the first term on the right-hand side of Eq. (9) is negative in its real part, whereas the second term is positive. The net behavior is illustrated in Fig. 2. It is inevitable that there is always a point where  $\text{Re}\langle \xi(\omega) \rangle$  vanishes, denoting the anti-resonance frequency. If we define a dynamic mass density<sup>1–3,7–9</sup> as

$$\rho_d = \frac{\langle f \rangle}{-\omega^2 \text{Re}\langle \xi \rangle}, \quad (10)$$

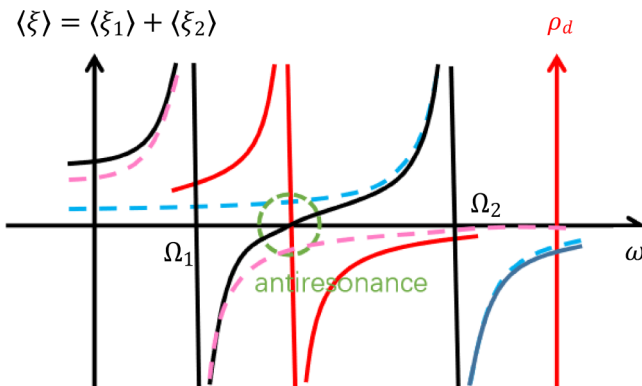


**FIG. 2.** An illustration of the displacement plotted as a function of frequency for the DMR. At a frequency intermediate between the two resonance frequencies, there is a point at which the displacement is zero. That point is denoted the anti-resonance frequency. The dynamic mass density as defined by Eq. (10) is plotted as the solid red line.

where  $\langle f \rangle$  denotes the area averaged force density, and the denominator is recognized to be the area-averaged acceleration. The behavior of  $\rho_d$  is also illustrated in Fig. 2, which is seen to display a nearly divergent behavior followed by a negative dynamic mass density region in which the acceleration is opposite to the force.

Can the divergence of the dynamic mass density have a real effect, in the sense of exhibiting consequences that imitate the effect of a large mass at the anti-resonance frequency? We show below that indeed, the dynamic mass density effect is real.

## 2. Coupling with propagating waves and evanescent waves—Total reflection at anti-resonance

Anti-resonance is associated with a special wave manipulation functionality of DMR.<sup>6</sup> To understand this functionality, we have to examine DMR's coupling to the incident and reflected waves. The basis of this consideration is a propagating wave's dispersion relation

$$k^2 = |\mathbf{k}_{||}|^2 + k_{\perp}^2 = \frac{\omega^2}{v_0^2} = \left( \frac{2\pi}{\lambda} \right)^2, \quad (11)$$

where  $\lambda$  denotes the wavelength in air, and subscripts  $||$  and  $\perp$  denote wavevector's components parallel and perpendicular to DMR's surface, respectively. The basis of our considerations is that the lateral dimension  $d$  of the DMR is subwavelength, i.e.,  $d \ll \lambda$ . For the resonance mode profiles depicted in Fig. 1, if we Fourier transform the two-dimensional mode profile to the transverse wavevector domain, then it is clear that except for one component of the transverse wavevector component that will be selected out for special note below, the other components must satisfy the inequality

$$|\mathbf{k}_{||}| > \frac{2\pi}{d} \gg \frac{2\pi}{\lambda}, \quad (12)$$

because all the lateral features of the resonance profile are smaller than  $d$ , and displacement is continuous across the membrane/air interface. That means in order to satisfy Eq. (11), the associated  $k_{\perp}$  must be purely imaginary, i.e., decaying away from the DMR surface exponentially and hence decoupled from the propagating waves. The one exception is the  $|\mathbf{k}_{||}| = 0$  component associated with the center of mass motion. Since  $|\mathbf{k}_{||}| = 0$  delineates a mode in which the whole DMR moves up and down in unison, we denote such a mode as the "piston mode." Hence for the DMR with subwavelength lateral dimensions, only the piston mode couples to the propagating modes since in that case we have  $k_{\perp} = k = 2\pi/\lambda$ .

Because at anti-resonance  $\langle \xi \rangle = 0$ , there is no piston mode and hence the DMR is decoupled from the propagating mode, i.e., it acts like a rigid wall and can totally reflect the acoustic wave at this frequency even though the DMR is a flimsy membrane. This effect has been experimentally demonstrated<sup>5</sup> as well as numerically simulated as shown in Fig. 3.

The total reflection behavior is consistent with the divergence of dynamic mass density as required by Eq. (10), i.e., at anti-resonance the DMR seems to acquire a very large mass density. In accordance to the mass density law, the transmission amplitude  $T$

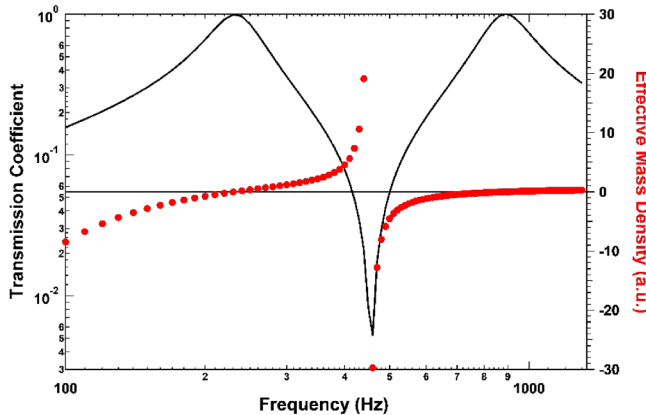


**FIG. 3.** Results of a full-waveform simulation on the DMR, with transmission coefficient shown as the black solid line. Full transmission is seen at the two resonances, with near-zero transmission at anti-resonance. The divergence of the dynamic mass density at anti-resonance is shown by solid red circles, as evaluated from Eq. (10) using simulated values for  $\xi$ . Adapted from Ref. 8.

of an acoustic wave through a solid wall with mass density  $\rho$  and thickness  $h$  is given by

$$T = i \frac{2Z_0}{\omega ph}, \quad (13)$$

independent of solid wall's bulk modulus. Hence, DMR's near-total reflection at anti-resonance is in agreement with the mass density law, by replacing the static mass density by the dynamic mass density in Eq. (13). Another manifestation of the large dynamic mass density at anti-resonance is the use of a very light-weight DMR in being able to successfully suppress vibration that is tuned to the antiresonance frequency.<sup>4</sup> As to the negative dynamic mass density, its effect was demonstrated in the first publication on locally resonant sonic materials.<sup>1–3,7</sup>

### 3. Acoustic absorption by DMR and its upper bound

Polymeric membranes usually have a low dissipation coefficient. However, absorption per unit volume is the product of energy density multiplied by the dissipation coefficient. In acoustic metamaterials, high absorption relies on a high energy density as the result of resonance, rather than the magnitude of the dissipation coefficient. In fact, a large dissipation coefficient can cause impedance mismatch with air, leading to increased reflection and reduced absorption as a result. In this context, a low dissipation coefficient may offer an advantage if properly utilized.

For the DMR, the largest energy density at resonance is located at the perimeter(s) of the solid mass, where there is a kink in the mode profile due to the large rigidity contrast between the solid and the membrane, as seen in Fig. 1. In this case, there can be a very large curvature energy density, localized at the perimeter(s), that is proportional to the square of the second derivative along the lateral direction, i.e.,  $\varepsilon \propto (\nabla_{||}^2 \xi)^2$ . Since a kink implies a discontinuity in the first derivative, the second derivative would resemble a

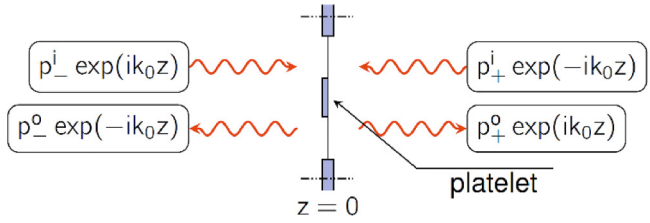


**FIG. 4.** An illustration of the incoming and outgoing acoustic waves on the two sides of the DMR, in terms of the pressure modulation. Here  $k_0 = \omega/v_0$ .

delta function. The delta function can be integrated to a finite value, but the square of the delta function implies a very large value even when integrated. A detailed finite element simulation has indeed confirmed this fact.<sup>11</sup> Hence, significant acoustic absorption by the DMR occurs at resonances through the curvature energy density enhancement by the resonant mode profile.

While the absorption by DMR can be significant, there exists an upper bound owing to the thin membrane thickness.<sup>12</sup> In order to see the inevitability of such a bound, let us consider two counter-propagating incoming waves incident from two sides on the DMR with pressure modulation amplitudes  $p_-^i$  and  $p_+^i$ . Upon reflection, they are converted into two outgoing waves with the relevant amplitudes  $p_-^o$  and  $p_+^o$ . The subscripts – and + denote the left- and right-hand side regions, respectively, and superscripts  $i$  and  $o$  stand for incoming and outgoing waves, respectively. In Fig. 4, we illustrate this incident and scattering configuration. At the surface of the DMR, the net pressure modulation is the sum of the incoming and outgoing pressure modulations. The time-averaged acoustic energy flux in air is given by  $pu/2 = \pm p^2/(2Z_0)$ , opposite in direction for the incident and outgoing waves. Owing to the small thickness of the membrane, we must have  $\langle u_- \rangle = \langle u_+ \rangle$ , i.e., the membrane thickness does not change since the membrane's thickness-varying resonance has a much higher frequency and, therefore, "frozen" in the relevant low frequency regime. As only the piston mode couples to the propagating waves and the displacement velocity is continuous between the coupling mode and air, we must have

$$\langle u_- \rangle = \frac{p_-^i - p_-^o}{Z_0} = \frac{p_+^o - p_+^i}{Z_0} = \langle u_+ \rangle. \quad (14)$$

As a note on the side, for a stationary solid boundary  $p_-^i = p_-^o$  so that the displacement velocity has a node, such as the case at anti-resonance. The total pressure on the solid boundary, on the other hand, is given by  $p_-^i + p_-^o$ . Hence, for a stationary wall the pressure exerted on the boundary is twice that of the incident wave.

### 4. Conservation law in analogy to momentum conservation

Equation (14) leads directly to the conservation law for the mean pressure modulation  $\bar{p}$ ,<sup>12</sup>

$$\bar{p} = \frac{1}{2}(p_+^i + p_-^i) = \frac{1}{2}(p_+^o + p_-^o). \quad (15)$$

Equation (15) is completely similar to the momentum conservation law before and after the collision between two identical particles. Here, we treat  $p_{+}^{i(o)}$  as complex numbers, or phasors, i.e., 2D vectors in the complex plane. The analog to the kinetic energy is the energy flux  $p^2/(2Z_0)$ .

It follows from analogy to classical mechanics that a wave incident from one side is just like the collision between a moving particle and a stationary one, with equal mass. In that case, half of the incident kinetic energy is the conserved center of mass energy and, therefore, not available for dissipation. Hence, the upper bound for DMR dissipation is 50%.

### 5. Hybrid structure and total absorption

From the simple argument that leads to the absorption upper bound for incidence from one side, it also becomes clear that if there are incident waves from both sides of the membrane, then 100% absorption is entirely possible. However, even if we have incidence only from one side, it is still possible to have backscattered wave from a reflecting surface on the other side. Hybrid resonance is the result of such considerations when the reflecting surface is placed in the near-field region (i.e., at a very subwavelength distance) to the DMR so that the resonance pattern of the DMR is altered as well.<sup>13</sup> In Fig. 5(a), we show such a configuration, denoted the *hybrid structure*, in which the DMR is subject to incident and scattered waves on the right,  $p_{+}^i$  and  $p_{+}^o$ , as well as similar waves on the left,  $p_{-}^i$  and  $p_{-}^o$ . However, the two waves on the right are subject to the reflecting boundary condition imposed by the hard wall placed at a distance  $s$  away from the DMR. Due to the hard wall boundary condition, the displacement velocity must have a node at the reflecting boundary. That means at the position of the DMR, the two waves on the right must have equal amplitude, i.e.,  $|p_{+}^i| = |p_{+}^o|$ , with a phase difference  $p_{+}^i/p_{+}^o = 2\delta = 2k_0s$ , where  $k_0 = \omega/v_0$ . The phase of  $p_{+}^o$  can be taken to be zero as the reference.

### 6. Imposition of the no-reflection condition

We wish to see if it is possible to achieve total absorption by the hybrid structure. Total absorption implies  $p_{-}^o = 0$ . Hence from

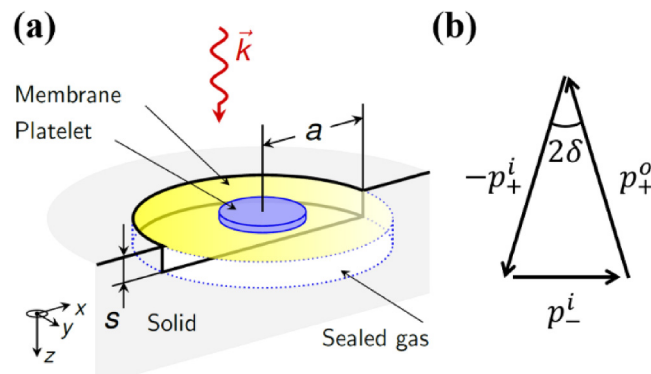


FIG. 5. (a) A pictorial illustration of the hybrid resonator structure. (b) A phasor diagram that illustrates Eq. (16) geometrically. Figure (a) adapted from Ref. 13.

Eq. (15), we have

$$p_{-}^i = p_{+}^o - p_{+}^i, \quad (16)$$

which can be represented by a phasor diagram as shown in Fig. 5(b) in which Eq. (16) is regarded as a two-dimensional vector equation in the complex plane, forming a closed triangle. Here, the phase is treated as giving the relative angle(s) between the vectors.

The net area-averaged pressure on the DMR is given by the difference between the two sides of the DMR:  $\langle p_{tot} \rangle = p_{-}^i - (p_{+}^o + p_{+}^i)$ . From Fig. 5(b), it is clear that  $p_{+}^o + p_{+}^i = ip_{+}^i \cot\delta$ . Hence,  $\langle p_{tot} \rangle = p_{-}^i(1 - \cot\delta)$ , and it follows that with the impedance condition imposed by  $p_{-}^o = 0$ , i.e., no reflection, the DMR impedance for total absorption needs to be

$$Z_{DMR} = \frac{\langle p_{tot} \rangle}{u} = \frac{p_{-}^i}{u}(1 - \cot\delta) = Z_0(1 - \cot\delta). \quad (17)$$

At the same time, we recognize that the impedance at the +side of the DMR, representative of the air cavity impedance that is in series with the DMR impedance, is precisely given by

$$Z_{cav} = \frac{p_{+}^o + p_{+}^i}{u} = iZ_0 \cot\delta. \quad (18)$$

When  $\delta \rightarrow 0$ ,  $Z_{cav} \rightarrow i\infty$  in agreement with that of a hard reflecting wall. It follows from Eqs. (17) and (18) that the total impedance of the hybrid structure is given by

$$Z_{hybrid} = Z_{DMR} + Z_{cav} = Z_0. \quad (19)$$

Since the reflection coefficient at normal incidence is given by

$$R = \frac{Z - Z_0}{Z + Z_0}, \quad (20)$$

hence consistency is achieved with the imposed no-reflection condition. We also note that from energy conservation the absorption is given by  $A = 1 - |R|^2$  when there is no transmission, it follows that  $Z = Z_0$  implies total absorption.

### 7. Emergence of hybrid resonance

A special situation occurs at  $\delta = (2n + 1)\pi/2$ , with  $n = 0, 1, \dots$ , or  $s = (2n + 1)\lambda/4$ . This is the “drum resonance” condition. However, if the reflecting wall is very close to the DMR, then it may seem impossible for total absorption to occur, unless DMR can exhibit an impedance that has a very large negative imaginary part. It turns out that precisely such an impedance can occur for the DMR at a frequency that is slightly less than the anti-resonance frequency. Just to make this point intuitively obvious, we note that from Eqs. (7) and (10), near the anti-resonance the impedance of the DMR can be expressed as

$$Z_{DMR} \propto -i\omega\rho_d, \quad (21)$$

apart from some constants. Since the dynamic mass density at frequencies less than the anti-resonance frequency can be very large

and positive, it follows that the condition imposed by the total absorption may indeed be realized close to the anti-resonance frequency. Such total absorption can be realized with significantly subwavelength sample thickness, thereby realizing the advantage of resonance-type acoustic metamaterials.

What is special and somewhat anti-intuitive about the hybrid resonance, is that there can be large membrane displacement even when the membrane is placed very close to a hard reflecting wall, which is always associated with a displacement velocity node. At low frequencies, any significant displacement velocity has to be at least a quarter of a wavelength away from the hard boundary, hence intuition would tell us that a membrane placed very close to a hard wall should have no displacement velocity at low frequencies. This intuition turns out to be wrong when the membrane has multiple resonance modes, with anti-resonances in-between any two resonances.

### 8. Mathematics of the hybrid mode

In a hybrid structure, the vibration modes of the DMR are altered in a manner such that the original modes are replaced by the hybrid resonances.<sup>13</sup> To see how the hybrid resonance actually emerge, we recall that the Green function can be expanded in terms of the eigenfunctions of the system. In the vicinity of the anti-resonance the Green function can be expressed as the sum of two Lorentzians,

$$\langle G \rangle = \sum_{n=1,2} \frac{|\langle \xi_n \rangle|^2}{m_n(\Omega_n^2 - \omega^2 - i\beta_n\omega)}, \quad (22)$$

where  $\xi_n(x_{||})$  denotes the displacement profile of the  $n$ th eigenfunction,

$$m_n = \frac{1}{\langle |\xi_n|^2 \rangle_A} \int_A \rho_a(x_{||}) |\xi_n(x_{||})|^2 dx_{||}. \quad (23)$$

Here  $A$  denotes the area of the membrane, and  $\rho_a(x_{||})$  is the area mass density, i.e., mass per unit area as a function of the planar coordinate. Consider the case where  $\beta_{1,2}/\omega \ll 1$  in the relevant frequency range, and for simplicity let  $\beta_1 = \beta_2$ . Then we can expand Eq. (22) as

$$\langle G \rangle = \sum_{n=1,2} \frac{|\langle \xi_n \rangle|^2}{m_n(\Omega_n^2 - \omega^2)} + 2i\beta \sum_{n=1,2} \frac{|\langle \xi_n \rangle|^2 \omega}{m_n(\Omega_n^2 - \omega^2)^2}. \quad (24)$$

This expansion is to facilitate the consideration that at the anti-resonance frequency  $\tilde{\omega}$ ,  $\text{Re}\langle G \rangle = 0$ . If we express the hybrid resonance frequency to be at  $\omega = \tilde{\omega} - \Delta\omega$ , where  $\Delta\omega/\tilde{\omega} \ll 1$ , then

$$\langle G \rangle \cong 2\Xi(i\beta - \Delta\omega), \quad (25)$$

where

$$\Xi = \sum_{n=1,2} \frac{|\langle \xi_n \rangle|^2 \tilde{\omega}}{m_n(\Omega_n^2 - \tilde{\omega}^2)^2}. \quad (26)$$

From Eq. (7), we obtain from Eq. (25)

$$Z = \frac{1}{2\beta\Xi} \frac{\beta - i\Delta\omega}{\beta^2 + \Delta\omega^2}. \quad (27)$$

If  $\beta \rightarrow 0$ , then the impedance diverges toward negative infinity when  $\Delta\omega \rightarrow 0$ . What we want, however, is for the real and imaginary parts of Eq. (27) to agree with those of Eq. (17),

$$Z_0 = \frac{1}{2\beta\Xi} \frac{\beta}{\beta^2 + \Delta\omega^2}, \quad (28a)$$

$$Z_0 \cot\delta = \frac{1}{2\beta\Xi} \frac{\Delta\omega}{\beta^2 + \Delta\omega^2}. \quad (28b)$$

These two conditions can certainly be satisfied since there are three adjustable parameters:  $\beta$ ,  $\Delta\omega$ , and  $\delta$ . Since  $\beta$  is a material parameter set by the material used, usually the tuning is carried out by adjusting the other two.

### 9. Profile of the hybrid resonance mode

At anti-resonance frequency we have the condition  $\text{Re}[\langle \xi_1 \rangle + \langle \xi_2 \rangle] = 0$ . Since the hybrid resonance frequency is only slightly less than  $\tilde{\omega}$ , at the hybrid resonance we must have  $|\langle \xi_1 \rangle| > |\langle \xi_2 \rangle|$  but  $|\langle \xi_2 \rangle|/|\langle \xi_1 \rangle| \approx 1$ . If in addition we impose the condition that the hybrid resonance's piston component amplitude must match that of the incident wave,  $\xi_s$ , in order to achieve impedance matching, then the following condition should hold:

$$\frac{|\langle \xi_h \rangle|}{|\langle \xi_1 \rangle|} = 1 - \frac{|\langle \xi_2 \rangle|}{|\langle \xi_1 \rangle|} = \frac{\xi_s}{|\langle \xi_1 \rangle|}. \quad (29)$$

As the right-hand side of Eq. (29) is a small number, it follows that  $|\langle \xi_1 \rangle|, |\langle \xi_2 \rangle| \gg |\langle \xi_h \rangle|$ , the piston mode amplitude of the hybrid mode. The implication is that the evanescent component of the hybrid resonance has a much larger displacement amplitude than that of the piston mode. In other words, for the hybrid resonance the variance of the displacement can be very large, i.e.,  $(\langle |\xi_h|^2 \rangle - |\langle \xi_h \rangle|^2)^{1/2} \gg |\langle \xi_h \rangle|$ . This has indeed been verified experimentally as seen in Fig. 6(a), together with the total absorption at hybrid resonance frequency of 152 Hz as shown in Fig. 6(b), both in excellent agreement with the theory simulation predictions.<sup>13</sup>

In the experiment, the sample thickness is noted to be more than two orders of magnitude smaller than the wavelength at 152 Hz, 2.3 m.

### C. Broadband optimal acoustic absorption structures

Resonance is inherently a dispersive, narrow frequency-width effect. In considering the practical applications of resonance-type acoustic metamaterials, this feature is a drawback since for most applications broadband functionality is a necessity. Therefore, how to achieve broadband functionality by integrating resonators with different resonance frequencies is a crucial concern for the development of acoustic metamaterials into useful products. Associated with this issue is the question whether acoustic metamaterials can still retain its advantage of subwavelength sample size in the broadband regime. We will see in this section that in regard to broadband acoustic

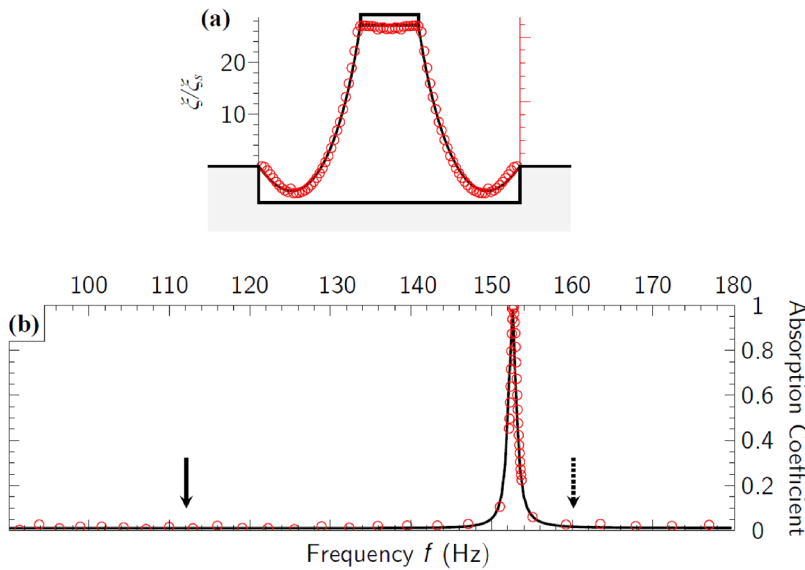


**FIG. 6.** (a) Numerical simulation of the hybrid mode, shown as the black line, plotted together with the laser vibrometer measurement of the hybrid mode's displacement, shown as empty red circles. It is seen that the ratio of the displacement to the incident wave's particle displacement,  $\xi_s$ , can be more than a factor of 20. Since hybrid resonance mode is impedance-matched to that of air,  $\xi_s$  is approximately equal to the piston mode component of the hybrid resonance's displacement profile. (b) Measured (plotted as red circles) and simulated (plotted as black line) absorption as a function of frequency. Total absorption is seen at 152 Hz. The solid arrow on the left indicates the frequency of the lowest resonance, the arrow with dashed line on the right indicates the anti-resonance frequency. Adapted from Ref. 13.

absorption functionality, the definition of metamaterial's advantage, as compared to the conventional absorption materials, is altered from the previous “subwavelength sample size.” We elaborate below.

Noise absorption is one of the most important application areas for acoustic metamaterials.<sup>16</sup> A thick-enough conventional acoustic absorbing materials, such as those used in anechoic chambers, can absorb acoustic waves of all frequencies; but the bulky unwieldiness limits their broad applications. In this regard an optimally integrated acoustic resonator structure can display the advantage of being able to target the spectrum range of peak noise, with a minimum sample thickness allowed by a law of nature—the causality constraint on minimum sample thickness associated with a given absorption spectrum.

### 1. Causality constraint on minimum sample thickness

Reflection and transmission of an incident wave are denoted the sample response to an incident wave. Since the incident wave varies as a function of time, the sample response will similarly acquire a time dependence. Causality is defined to mean that the response at any given moment can only depend on what transpired prior to that moment, but not on anything that happens after that moment, i.e., the future cannot affect what is happening now. When translated into mathematical language, this simple and intuitive statement led to some marvellous results. The most famous one is the Kramers–Kronig relation, taught in almost all the standard electrodynamics textbooks, that relates the real and imaginary parts of the electromagnetic dielectric constant in the frequency domain. A less-known consequence is the inequality constraint that relates the absorption spectrum to a minimum sample thickness. Since its derivation can be found in the literature<sup>14</sup> and is beyond the scope of this tutorial, we just state it below as a simple inequality,

$$d \geq \frac{1}{4\pi^2} \frac{B_{\text{eff}}}{B_0} \left| \int_0^\infty \ln[1 - A(\lambda)] d\lambda \right| = d_{\min}, \quad (30)$$

where  $d$  is the sample thickness,  $A(\lambda)$  is the absorption spectrum,  $B_{\text{eff}}$  denotes the effective bulk modulus of the sound absorbing structure in the static limit, and  $B_0$  is the bulk modulus of air. Two implications of Eq. (30) are (a) low frequency absorption inherently requires a larger sample thickness as compared to absorption at higher frequencies, and (b) any given absorption spectrum is associated with a minimum sample thickness. We denote “optimal” those absorption structures or materials that can nearly attain equality with  $d_{\min}$ .

The causality constraint serves as the reference for judging the “degree of success” of a broadband absorption material/structure. It also tells us that for a given sample thickness, there is only a finite amount of wave absorption resources available. Hence how to allocate the absorption resources, in the form of an absorption spectrum, is an issue of importance. If the aim is to absorb noise, then the best allocation strategy is naturally to match the absorption spectrum with the noise spectrum. The freedom offered by an integrated array of acoustic resonators in realizing a target absorption spectrum is therefore the main advantage over the conventional absorption materials, which are otherwise excellent in their acoustic absorption capabilities. Since the low frequency noise in the range of less than 500–1000 Hz is the most difficult to absorb with a reasonable sample thickness, it is in this range that acoustic metamaterial can be most effective.

### 2. Fabry–Pérot resonators

An acoustic Fabry–Pérot (FP) resonator is just a hollow pipe with subwavelength cross sectional dimension. One end of the pipe is closed with a hard reflecting boundary; the other end is open. The boundary condition at the closed end—displacement velocity node—means that the displacement velocity has the following functional form:

$$u(z) = u_0 \sin \left[ \frac{\omega}{v_0} (\ell - z) \right], \quad (31a)$$

where  $\ell$  is the length of the FP resonator,  $u_0$  is the amplitude of incident wave's displacement velocity, and  $z=0$  is taken to be the position of the open mouth end of the resonator. Here the time dependence,  $\exp(-i\omega t)$ , is always implied. From Eq. (31a) and Eq. (3), we obtain the pressure modulation as

$$p(z) = iZ_0 u_0 \cos \left[ \frac{\omega}{v_0} (\ell - z) \right]. \quad (31b)$$

The impedance at the mouth of the FP resonator as perceived by the incident wave, is given by

$$z = \frac{p(0)}{u(0)} = iZ_0 \cot \left( \frac{\omega}{v_0} \ell \right), \quad (32a)$$

which is identical to Eq. (18) with  $\delta = \omega\ell/v_0$ . Here we use the lower-case  $z$  to denote the impedance of a single FP resonator, in anticipation of later development below where we use  $Z$  to denote the impedance of a sample comprising an array of integrated FP resonators. Similarly, we use lower-case  $g$  to denote the Green function of a single resonator so that

$$z = \frac{1}{-i\omega g}. \quad (32b)$$

The upper-case  $G$  will be used for the Green function of an integrated array of FP resonators.

The fact that a hollow pipe can be a resonator, i.e., with the Lorentzian form, becomes clear with the following mathematical identity:

$$\tan \left( \frac{\pi x}{2} \right) = \frac{4x}{\pi} \sum_{m=1}^{\infty} \frac{1}{(2m-1)^2 - x^2}. \quad (33)$$

By comparing the arguments of cotangent in Eq. (32) with the tangent in Eq. (33), we obtain  $x = 4\ell/\lambda$ . In Eq. (33)  $x = 2m-1$  indicates the condition for a resonance, hence  $\Omega^{(m)} = (2m-1)(\pi v_0/2\ell) = (2m-1)\Omega$  are the FP resonance frequencies. The lowest resonance frequency  $\Omega$ , with  $m=1$ , corresponds with the condition  $\ell = \lambda/4$ , i.e.,

$$\ell = \frac{\pi v_0}{2\Omega}. \quad (34)$$

By adding a vanishingly small imaginary part in the denominator of Eq. (33), we obtain after some re-arrangement the following expression:

$$\frac{Z_0}{z} = -i \lim_{\beta \rightarrow 0} \sum_{m=1}^{\infty} \frac{4\omega\Omega/\pi}{(2m-1)^2\Omega^2 - \omega^2 - i\beta\omega}, \quad (35)$$

which is in full accordance with the Lorentzian expression for multiple resonances in a FP resonator. From Eqs. (8) and (35)

can be further reduced to the form

$$\frac{Z_0}{z} = -iP \sum_{m=1}^{\infty} \frac{4\omega\Omega/\pi}{(2m-1)^2\Omega^2 - \omega^2} + \sum_{m=1}^{\infty} 2\Omega\delta[(2m-1)\Omega - \omega]. \quad (36)$$

### 3. Integration scheme with a continuum of FP resonators to achieve tunable absorption spectrum

In order to obtain broadband absorption, integration by using an array of FP resonators is a necessity. However, using FP resonators with equally spaced (lowest order) frequencies is not the best strategy to obtain, for example, a flat absorption spectrum. Instead, there is an integration strategy<sup>14,15</sup> that can best achieve a target absorption spectrum, shown below.

Consider a continuum of  $\Omega$  in an idealized FP resonator array. The lateral size of the array will be assumed to be smaller than the relevant wavelength in the following discussion. Since these resonators are arranged in parallel, the array impedance is the sum of the inverse of the individual impedances. In addition, we assume that the FP resonators are separated by hard reflecting surfaces that occupy a fraction  $1-\varphi$  of the total surface area exposed to the incident wave. Since the inverse of the hard reflecting surface impedance is zero, hence the FP resonator array has a real part of the inverse impedance given by

$$\frac{Z_0}{Z} = \int_{\Omega_C}^{\infty} \sum_{m=1}^{\infty} 2\Omega\varphi D(\Omega)\delta[(2m-1)\Omega - \omega]d\Omega, \quad (37)$$

where  $\Omega_C$  is a lower cut-off frequency as required by the causality constraint in order for the array to have a finite sample thickness. Here, we have inserted a mode density

$$D(\Omega) = \frac{dn}{d\Omega}, \quad \Omega > \Omega_C, \quad (38a)$$

$$D(\Omega) = 0, \quad \Omega \leq \Omega_C \quad (38b)$$

in the integral. Here,  $n$  is treated as a continuous real number that can be viewed as the index  $\tilde{n}$  of  $N$  resonators to span a finite, fixed frequency range. As  $N$  approaches infinity,  $\tilde{n}/N \rightarrow n$ . We will see that the determination of the mode density is the central task of the integration scheme, with the goal of attaining the target absorption spectrum.

In Eq. (37), we have purposely ignored the imaginary part of the inverse impedance because that part is oscillatory as a function of  $\Omega$  and, therefore, its integrated effect will be minimal. However, the imaginary part of the inverse impedance will be fully taken into account after the mode density is determined so that the full integration of the Lorentzian form can be carried out with the complex denominator. It will be seen that the effect of including the imaginary part is to introduce a smooth transition region above the cutoff that tends exponentially to the designed absorption spectrum.

By carrying out the integration in Eq. (37), we obtain a simple expression

$$\frac{Z_0}{Z(\omega)} = \sum_{m=1}^{\infty} \left[ \frac{2\varphi\Omega D(\Omega)}{2m+1} \right]_{\Omega=\frac{\omega}{2m-1}}, \quad \Omega > \Omega_C. \quad (39)$$

At this point, it is instructive to first illustrate the determination of mode density from the target absorption spectrum by ignoring all terms on the right-hand side of Eq. (39) with  $m \geq 2$ , i.e., retaining only the lowest-order FP resonances. From Eq. (38a) and the condition  $\Omega = \omega$ , we have

$$\frac{d\Omega}{dn} = 2\varphi\Omega \left( \frac{Z}{Z_0} \right), \quad (40)$$

where the quantity  $(Z/Z_0)$  is treated as the *known input*, determined from the target absorption spectrum  $A(\omega) = 1 - |[Z(\omega) - Z_0]/[Z(\omega) + Z_0]|^2$ . Here, we would like to treat the simplest case of total absorption above the cutoff frequency, by letting  $Z/Z_0 = 1$ . In that case, the solution of Eq. (40) is an exponential

$$\Omega = \Omega_C \exp[2\varphi n], \quad (41)$$

where we used the initial condition  $\Omega = \Omega_C$  at  $n = 0$ . It should be noted that in accordance to the inverse relationship between  $\Omega$  and  $\ell$ , Eq. (41) or its improved version by including all the higher-order FP resonances (see below), determines FP resonators' length distribution provided  $\varphi$  is known. In anticipation of later development, here we mention that there is indeed an optimal value of  $\varphi$ , fixed by using the causality constraint's minimum sample thickness  $d_{\min}$ .

It should be noted that if the target absorption spectrum is not total absorption, then Eq. (40) represents a somewhat more difficult differential equation to solve, but should be able to be solved numerically if the given  $Z/Z_0$  is frequency dependent.

#### 4. Correction to the resonator frequency distribution by including higher-order FP resonances

Equation (39) can be written in the form of

$$\frac{Z_0}{Z} = \sum_{m=1}^{\infty} \frac{a[\omega/(2m-1)]}{2m-1} = a(\omega) + \frac{1}{3}a\left(\frac{\omega}{3}\right) + \frac{1}{5}a\left(\frac{\omega}{5}\right) + \dots, \quad (42a)$$

where the left-hand side is treated as known. By comparison with Eq. (39), it can be seen that

$$a\left(\frac{\omega}{2m-1}\right) = \left[ 2\Omega\varphi \frac{dn}{d\Omega} \right]_{\Omega=\frac{\omega}{2m-1}}, \quad (42b)$$

and since there is no mode density below  $\Omega_C$ , we have the condition

$$a\left(\frac{\omega}{2m-1}\right) = 0, \quad \text{if } \frac{\omega}{2m-1} < \Omega_C. \quad (42c)$$

Provided that the left-hand side of Eq. (42b) can be solved in terms of the input  $(Z_0/Z)$ , then the distribution of resonator frequencies can be solved in terms of a first order differential equation. Below, we illustrate the solution of this problem in the case of total absorption, i.e.,  $Z_0/Z = 1$ .

In view of the  $2m-1$  factor in the series, Eq. (42a), the solution proceeds in discrete frequency segments. For  $\Omega_C < \omega < 3\Omega_C$ , we have  $1 = a(\omega) + 0 + \dots$  since for  $\omega/(2m-1)$  with  $m > 1$   $a(\omega/(2m-1)) = 0$  in accordance to Eq. (42c). Therefore,  $a(\omega) = 1$  for  $\Omega_C < \omega < 3\Omega_C$ , denoted as  $a_1$ . For  $3\Omega_C < \omega < 5\Omega_C$ , we have  $1 = a(\omega) + (1/3) \times a(\omega/3) + 0 + \dots = a(\omega) + (1/3) \times 1 + 0 + \dots$ . Therefore,  $a(\omega) = 2/3$  for  $3\Omega_C < \omega < 5\Omega_C$ , denoted as  $a_2$ . For  $5\Omega_C < \omega < 7\Omega_C$  we have  $1 = a(\omega) + (1/3) \times a(\omega/3) + (1/5) \times a(\omega/5) + \dots = a(\omega) + (1/3) \times 1 + (1/5) \times 1$ . Therefore  $a(\omega) = 7/15$  for  $5\Omega_C < \omega < 7\Omega_C$ , denoted as  $a_3$ .

It follows from above that in every frequency segment all terms of the series except the first one,  $m = 1$ , are either zero as required by the condition set by Eq. (42c), or fixed by the previous frequency segments. Since for  $m = 1$  we have  $\omega = \Omega$ , hence the value of  $a(\Omega)$  for all frequencies  $\Omega/\Omega_C$  can be uniquely fixed. This is shown in Fig. 7. Since in the  $m$ th frequency segment  $a_m$  is a constant, the differential equation has the simple form

$$\frac{d\Omega}{dn} = \frac{2\varphi\Omega}{a_m}. \quad (43)$$

The solution for the total absorption case is, therefore, given by

$$\Omega = (2m-1)\Omega_C \exp[2\varphi a_m^{-1}n], \quad (2m-1)\Omega_C < \Omega < (2m+1)\Omega_C, \quad (44)$$

where  $\max[n] = \ell n[(2m+1)/(2m-1)]/2\varphi a_m^{-1}$ .

In Fig. 8, we plot  $\ln(\Omega/\Omega_C)$  as a function of  $n$  for an arbitrary value of  $\varphi = 0.98$ . It is seen that the correction by including all the higher order FP resonances has the effect of making resonator's frequency distribution super-linear in the logarithmic plot. Here, the red dots indicate the best discrete choice of the resonator frequencies to achieve total absorption.

Again, if the target absorption spectrum differs from total absorption, then the solution to Eqs. (42) and (43) needs to be modified to take into account the frequency dependence of the input  $Z/Z_0$ .

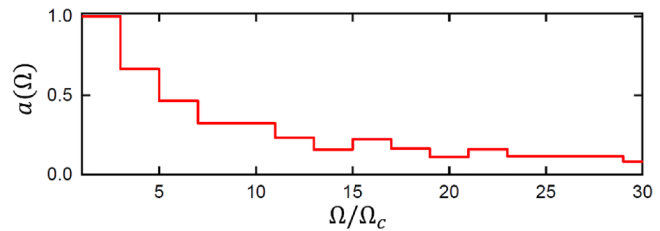


FIG. 7. The value of solved  $a(\Omega)$  plotted as a function of  $\Omega/\Omega_C$ .

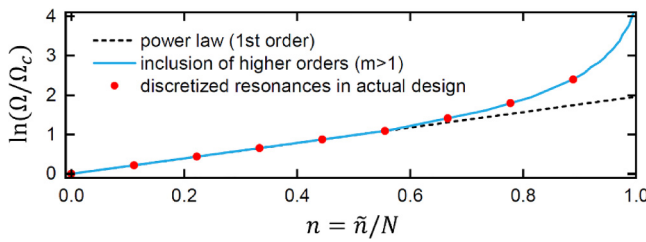


FIG. 8. Logarithm of the resonator frequency plotted as a function of  $n$ . The dashed line indicates the exponential relation obtained by ignoring all the higher order FP resonances. The solid red circles indicate the best choice for the (lowest order) FP resonator frequencies for a 3 by 3 array.

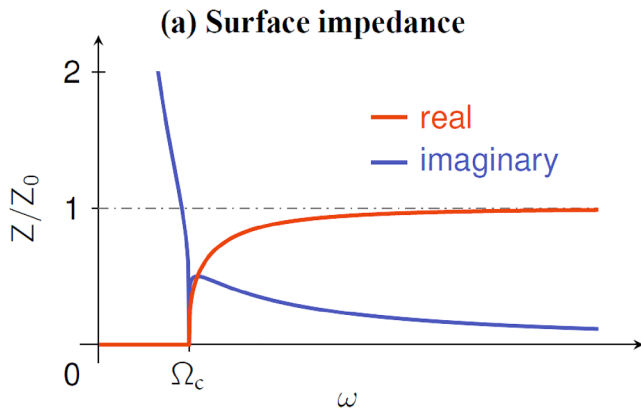
### 5. Inclusion of the imaginary part of the impedance

In the pursuit of the best design for the resonator integration, we have so far ignored the imaginary part of the impedance as pointed out above. Here, we return to Eq. (35) to carry out the integration over  $\Omega$ ,

$$\frac{Z_0}{Z} = -i \frac{2\omega}{\pi} \lim_{\beta \rightarrow 0} \int_{\Omega_C}^{\infty} \frac{\sum_{m=1}^{\infty} 2\Omega \varphi D(\Omega)/(2m-1)}{\tilde{\Omega}^2 - \omega^2 - i\beta\omega} d\tilde{\Omega}, \quad (45)$$

where  $\tilde{\Omega} = (2m-1)\Omega$  and by the definition of a lower cutoff,  $\tilde{\Omega}_C = \Omega_C$ . For the total absorption case, the numerator inside the integral is equal to 1 in accordance to the designed resonance frequency distribution. By using Eq. (8), the resulting integration can be done exactly to yield the impedance expression

$$\frac{Z(\omega)}{Z_0} = \left[ 1 - \frac{2i}{\pi} \operatorname{arctanh} \left( \frac{\Omega_C}{\omega} \right) \right]^{-1}, \quad \omega > \Omega_C, \quad (46a)$$



$$\frac{Z(\omega)}{Z_0} = i\pi \left[ \ell n \left( \frac{\Omega_C + \omega}{\Omega_C - \omega} \right) \right]^{-1}, \quad \omega < \Omega_C. \quad (46b)$$

In Eq. (46b), we have taken  $\ell n(-1) = -i$  in order to cancel out the real part of the impedance as it should vanish, since there is no mode density below the cutoff frequency. The real and imaginary parts of the impedance are plotted in Fig. 9(a). The resulting absorption spectrum is plotted in Fig. 9(b), where  $A(\omega) = 1 - |(Z(\omega)/Z_0 - 1)/(Z(\omega)/Z_0 + 1)|^2$ . It is seen that indeed the effect of the imaginary part decays quickly above the cutoff frequency as stated earlier but induces a smooth exponential approach to the target absorption spectrum.

### 6. Circle of consistency and the determination of optimal $\varphi$

In the above, sample thickness is only implicitly implied by the distribution of  $\Omega$ , as the FP resonator's length is specified by Eq. (34). If the longer FP resonators can be folded so that the overall shape of the sample is a compact cuboid, then its thickness should be given by the average of all the FP resonator lengths as dictated by volume conservation. We denote the average as  $\bar{\ell}$ . As  $\varphi$  is present in the  $\Omega$  distribution, Eqs. (41) or (44),  $\bar{\ell}$  is, therefore, a function of  $\varphi$ . By equating  $\bar{\ell} = d_{\min}$ , the value of  $\varphi$  can be explicitly determined. We illustrate below this process in the simple case of Eq. (41) where only the lowest-order FP resonances are taken into account. From Eqs. (34) and (41), we obtain from  $\bar{\ell} = d_{\min}$  the following condition:

$$d_{\min} = \bar{\ell} = \frac{\pi v_0}{2N\Omega_c} \sum_{n=1}^N \exp[-2\varphi(\tilde{n}-1)/N] \cong \frac{\pi v_0}{4\phi\Omega_c} [1 - \exp(-2\varphi)]. \quad (47)$$

On the other hand, we can use Eqs. (46) and (30) to calculate  $d_{\min} = 2v_0/\pi\varphi\Omega_c$ , where we have used the effective medium

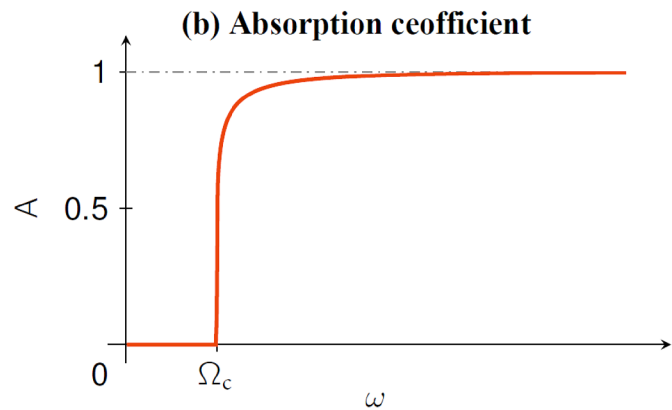


FIG. 9. (a) The real (in red) and imaginary (in blue) parts of the impedance, plotted as a function of frequency. (b) Absorption coefficient evaluated from the impedance shown in (a). Imaginary part of the impedance is shown to have a minor effect above the cutoff frequency. Adapted from Ref. 14.

expression  $B_{eff} = B_0/\varphi$ . This leads to the optimal value

$$\varphi = -\frac{1}{2}\ell \ln(1 - 8/\pi^2) = 0.832. \quad (48)$$

A similar optimal value of  $\varphi = 0.982$  may be obtained by considering the correction due to the higher order FP resonances. This final piece of design strategy completes the “circle of consistency” depicted by Fig. 10.

### 7. Self-energy correction

Consider a square array of a finite number of FP resonators, each with a different  $\Omega$ . Let  $g_{\tilde{n}}$  denote the Green function of the  $\tilde{n}$ th resonator. The pressure at the mouth of the resonators must be different in accordance with Eq. (31b) when excited, e.g., at a frequency intermediate between two (lowest order) resonances. With a pressure difference, there must be lateral air flow. This implies the different resonators to be essentially interacting with each other, i.e., they constitute an interacting system. When that happens, the Green function of each resonator will be renormalized with the consequence that the resonance frequency of each resonator is shifted downward somewhat. The kernel of such interaction renormalization is called self-energy,<sup>14</sup> adapted from the Dyson equation terminology for a multi-entity interacting system. Also, the lateral oscillating air flow implies evanescent waves that decay away from the array surface, and such evanescent waves with their attendant lateral air flows can be utilized to smooth out the absorption spectrum of an array with an insufficient, finite number of resonators; e.g., by putting a thin layer of acoustic sponge over the surface of the array.

To obtain an explicit expression for the self-energy, we observe that the displacement velocity  $u_{\tilde{n}}$  at the mouth of the  $\tilde{n}$ th resonator can be expressed as

$$u_{\tilde{n}} = -i\omega g_{\tilde{n}}(\langle p \rangle + \delta p_{\tilde{n}}), \quad (50)$$

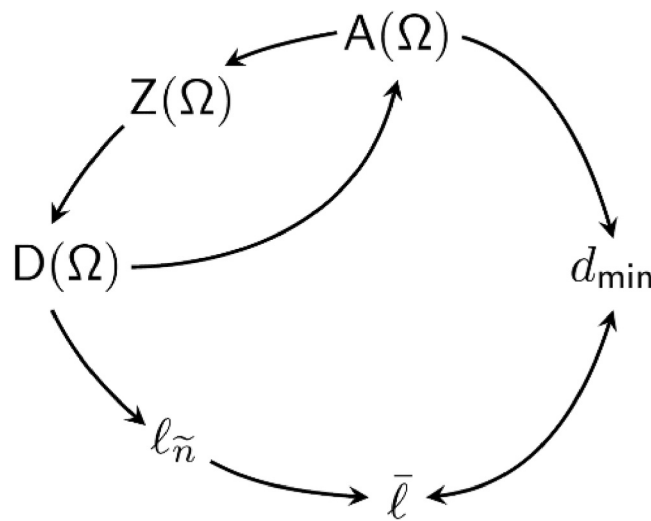


FIG. 10. The circle of consistency that closes the loop. Adapted from Ref. 15.

where  $\langle p \rangle$  is the modulation pressure averaged over the array surface, and  $\delta p_{\tilde{n}}$  denotes the local deviation from the average, arising from the evanescent modes. Hence,  $\langle \delta p_{\tilde{n}} \rangle = 0$ . Since collectively  $\delta p_{\tilde{n}}$ 's are associated with evanescent waves that exponentially decay away from the array surface, one should be able to express  $\delta p_{\tilde{n}} = \delta p(\mathbf{x}_{||}^{(\tilde{n})})$  in the wavevector domain by using the normalized Fourier basis  $\gamma_{\alpha}(\mathbf{x}_{||}) = \exp(-i\mathbf{k}_{||}^{(\alpha)} \cdot \mathbf{x}_{||})$ . Effectively, that means  $\delta p(\mathbf{x}_{||}) = \sum_{\alpha} \delta p(\mathbf{k}_{||}^{(\alpha)}) \gamma_{\alpha}(\mathbf{x}_{||})$ . Here, the wavevectors  $\mathbf{k}_{||}^{(\alpha)}$  are discretized by the condition that  $\gamma_{\alpha}(\mathbf{x}_{||})$  integrated over the array surface must vanish, with index  $\alpha = (\alpha_x, \alpha_y)$ ,  $\alpha_x, \alpha_y = \pm 1, \pm 2, \dots$ . That means  $|\mathbf{k}_{||}^{(\alpha)}| = (2\pi/L)\sqrt{\alpha_x^2 + \alpha_y^2}$ , where  $L$  denotes the side length of the square array. The reason for expressing  $\delta p$  in the wavevector domain is to obtain the  $z$  variation of the evanescent mode. Since the lateral size of the array is smaller than the relevant incident wavelength, we must have  $|\mathbf{k}_{||}^{(\alpha)}| > \omega/v_0$ . Hence, it follows from Eq. (11) that  $k_{\perp} = \sqrt{|\mathbf{k}_{||}^{(\alpha)}|^2 - (\omega/v_0)^2}$  is indicative of the exponential decay length of the evanescent wave. It follows that

$$\delta p(\mathbf{x}_{||}, z) = \sum_{\alpha} \delta p(\mathbf{k}_{||}^{(\alpha)}) \gamma_{\alpha}(\mathbf{x}_{||}) \exp\left(-\sqrt{|\mathbf{k}_{||}^{(\alpha)}|^2 - (\omega/v_0)^2}|z|\right). \quad (51)$$

The  $z$  variation of pressure modulation implies that from Eq. (3), we have at  $z=0$ ,

$$\sum_{\alpha} \delta p(\mathbf{k}_{||}^{(\alpha)}) \gamma_{\alpha}(\mathbf{x}'_{||}) \sqrt{|\mathbf{k}_{||}^{(\alpha)}|^2 - (\omega/v_0)^2} = i\omega\rho_0 \delta u(\mathbf{x}'_{||}), \quad (52)$$

where  $\delta u(\mathbf{x}'_{||}) = u(\mathbf{x}'_{||}) - \langle u(\mathbf{x}'_{||}) \rangle$ . The Fourier component  $\delta p(\mathbf{k}_{||}^{\beta})$  can be solved in terms of  $\delta u(\mathbf{x}_{||})$  by using the orthogonality property of the Fourier basis. The result is

$$\delta p(\mathbf{k}_{||}^{\alpha}) = i\omega\rho_0 \frac{\frac{1}{L^2} \int_{surface} u(\mathbf{x}'_{||}) \gamma_{\alpha}^{*}(\mathbf{x}'_{||}) d\mathbf{x}'_{||}}{\sqrt{|\mathbf{k}_{||}^{(\alpha)}|^2 - (\omega/v_0)^2}}. \quad (53)$$

We observe that the integral of  $\langle u(\mathbf{x}'_{||}) \rangle \gamma_{\alpha}^{*}(\mathbf{x}'_{||})$  must vanish, owing to the condition imposed on the Fourier basis, hence  $\delta u(\mathbf{x}'_{||})$  can be replaced by  $u(\mathbf{x}'_{||})$  in Eq. (53). By substituting Eq. (53) into Eq. (51) and setting  $z=0$ , we obtain

$$\begin{aligned} \delta p(\mathbf{x}_{||}, z=0) &= \frac{i\omega\rho_0}{L^2} \int_{surface} \left( \sum_{\alpha} \frac{\gamma_{\alpha}(\mathbf{x}_{||}) \gamma_{\alpha}^{*}(\mathbf{x}'_{||})}{\sqrt{|\mathbf{k}_{||}^{(\alpha)}|^2 - (\omega/v_0)^2}} \right) u(\mathbf{x}'_{||}) d\mathbf{x}'_{||} \\ &= \frac{i\omega\rho_0}{L^2} \int_{surface} \Lambda(\mathbf{x}_{||}, \mathbf{x}'_{||}) u(\mathbf{x}'_{||}) d\mathbf{x}'_{||}. \end{aligned} \quad (54)$$

Equation (54) can be easily expressed in a discretized form as

$$\delta p_{\tilde{n}} = i\omega\rho_0 \sum_{\tilde{m}} \Lambda_{\tilde{n}\tilde{m}} u_{\tilde{m}}, \quad (55)$$

with  $\tilde{n}$ ,  $\tilde{m}$  being the discrete indices of the resonators in the array. Just to be self-contained, we give below the expression for  $\Lambda_{\tilde{n}\tilde{m}}$ ,

$$\Lambda_{\tilde{n}\tilde{m}} = \frac{1}{N} \frac{\left( \frac{1}{\sigma_{\tilde{n}}} \int_{\sigma_{\tilde{n}}} \gamma_\alpha(\mathbf{x}_{||}) d\mathbf{x}_{||} \right) \left( \frac{1}{\sigma_{\tilde{m}}} \int_{\sigma_{\tilde{m}}} \gamma_\alpha(\mathbf{x}'_{||}) d\mathbf{x}'_{||} \right)}{|\mathbf{k}_\alpha|}, \quad (56)$$

where  $N$  is the total number of resonators in the array, and the integrals are to be carried out over the cross-sectional areas of the mouths for resonators  $\tilde{n}$  and  $\tilde{m}$ , with  $\mathbf{x}_{||}^{(\tilde{n})}$ ,  $\mathbf{x}'_{||}^{(\tilde{m})}$  being their respective center positions. Here,  $\sigma_{\tilde{n}}$  denotes the mouth area of resonator  $\tilde{n}$ , and we have assumed  $|\mathbf{k}_\alpha| \gg \omega/v_0$ . By carrying out the integrations, we obtain

$$\Lambda_{\tilde{n}\tilde{m}} = N \sum_{\alpha} \frac{\sin^2(\alpha_x \pi / \sqrt{N}) \sin^2(\alpha_y \pi / \sqrt{N})}{\pi^4 \alpha_x^2 \alpha_y^2 |\mathbf{k}_\alpha|} \exp[i\mathbf{k}_\alpha \cdot (\mathbf{x}_{||}^{(\tilde{n})} - \mathbf{x}_{||}^{(\tilde{m})})]. \quad (57)$$

Equations (50) and (55) are the starting point of an infinite series as can be seen as follows. By substituting Eq. (55) into Eq. (50), one obtains

$$u_{\tilde{n}} = -i\omega g_{\tilde{n}} (\langle p \rangle + i\omega\rho_0 \sum_{\tilde{m}} \Lambda_{\tilde{n}\tilde{m}} u_{\tilde{m}}). \quad (58)$$

But, then one can substitute Eq. (50) into the right-hand side of Eq. (58) to obtain

$$u_{\tilde{n}} = -i\omega g_{\tilde{n}} \left( \langle p \rangle + \omega^2 \rho_0 \sum_{\tilde{m}} \Lambda_{\tilde{n}\tilde{m}} g_{\tilde{m}} (\langle p \rangle + \delta p_{\tilde{m}}) \right). \quad (59)$$

At this point, it is already clear that by repeated, alternating substitutions, one can obtain the following series:

$$u_{\tilde{n}} = -i\omega \left[ g_{\tilde{n}} + \left( (\omega^2 \rho_0 g_{\tilde{n}}^2 \Lambda_{\tilde{n}\tilde{n}} + \omega^4 \rho_0^2 g_{\tilde{n}}^3 \Lambda_{\tilde{n}\tilde{n}}^2 + \dots) + \sum_{\tilde{m}} \Pi_{\tilde{n}\tilde{m}} \right) \right] \times \langle p \rangle, \quad (60)$$

where we have separated out the diagonal terms in the  $\{\Lambda_{\tilde{n}\tilde{m}}\}$  matrix. The off-diagonal terms are grouped into the term  $\Pi_{\tilde{n}\tilde{m}}$ , with  $\tilde{n}$  not equal to  $\tilde{m}$ . It is found that  $\Pi_{\tilde{n}\tilde{m}}$  is order(s) of magnitude smaller than the diagonal terms due to the summation over the oscillation phase factors, hence it can be neglected. By retaining only the diagonal terms, we obtain

$$\begin{aligned} u_{\tilde{n}} &= -i\omega \left( g_{\tilde{n}} + \frac{\omega^2 \rho_0 g_{\tilde{n}}^2 \Lambda_{\tilde{n}\tilde{n}}}{1 - \omega^2 \rho_0 g_{\tilde{n}} \Lambda_{\tilde{n}\tilde{n}}} \right) \langle p \rangle \\ &= -i\omega \left( \frac{g_{\tilde{n}}}{1 - \omega^2 \rho_0 g_{\tilde{n}} \Lambda_{\tilde{n}\tilde{n}}} \right) \langle p \rangle \\ &= -i\omega \frac{1}{g_{\tilde{n}}^{-1} - \omega^2 \rho_0 \Lambda_{\tilde{n}\tilde{n}}} \langle p \rangle. \end{aligned} \quad (61)$$

For the incident wave, the perceived effective impedance for the  $\tilde{n}$  th oscillator is given by

$$z_{\tilde{n}} = \frac{\langle p \rangle}{u_{\tilde{n}}} = \frac{1}{-i\omega g_{\tilde{n}}^{(e)}}, \quad (62)$$

where we have defined  $g_{\tilde{n}}^{(e)}$  to be the renormalized effective Green function for the  $\tilde{n}$  th oscillator. Comparison of Eq. (62) to Eq. (61) leads to the Dyson equation

$$(g_{\tilde{n}}^{(e)})^{-1} = g_{\tilde{n}}^{-1} - \omega^2 \rho_0 \Lambda_{\tilde{n}\tilde{n}}, \quad (63)$$

from which we identify the self-energy correction to be  $\omega^2 \rho_0 \Lambda_{\tilde{n}\tilde{n}}$ . Since the resonance frequency is generally identified by the vanishing of the real part of  $g_{\tilde{n}}^{-1}$ , it follows that the self-energy renormalization has the effect of shifting the resonance frequency to where the real part of  $(g_{\tilde{n}}^{(e)})^{-1}$  vanishes. It should be noted that in accordance to Eq. (57), if  $N \rightarrow \infty$ , then  $\Lambda_{\tilde{n}\tilde{n}} \rightarrow 0$ . Therefore, the self-energy correction is inherently an effect associated with a finite number of resonators.

Since the resonators' impedances are in parallel, the sample impedance for the array is given by

$$\frac{1}{Z} = \sum_{\tilde{n}} \frac{f_{\tilde{n}}}{z_{\tilde{n}}} = \sum_{\tilde{n}} f_{\tilde{n}} (-i\omega g_{\tilde{n}}^{(e)}), \quad (64)$$

where  $f_{\tilde{n}}$  is the area fraction occupied by the mouth area of the resonator, with  $\sum f_{\tilde{n}} = \varphi$ . If the resonators have the same cross-sectional area, then  $f_{\tilde{n}} = \varphi/N$  so that

$$Z = \frac{i}{\omega} \left( \frac{\varphi}{N} \sum_{\tilde{n}=1}^N g_{\tilde{n}}^{(e)} \right)^{-1}. \quad (65)$$

## 8. Experimental verification

In Fig. 11(a), we show a schematic picture and a photo image of the sample. The array has 16 resonators whose  $\Omega$ 's are designed in accordance with the total absorption target spectrum with a cutoff frequency set at 345 Hz. The photo image actually shows four such arrays, each one in the shape of a compact cuboid that is 10.6 cm in thickness and approximately 2.3 cm by 2.3 cm in cross-sectional dimension. The longer FP channels were folded so that the cuboid thickness is very close to  $\ell$ . Since 16 resonators were insufficient to produce a flat absorption spectrum, a 3 mm thick sponge was put on top of the array surface in order to utilize the lateral air flows of the evanescent modes for filling the dips in the

absorption spectrum. The absorption results measured by using the impedance tube are shown as open circles in Fig. 11(b). The idealized target spectrum is shown by the red dashed line, and the theory prediction from Eq. (65), by using parameter values detailed in Ref. 14, is shown as the solid red line. Excellent agreement is seen. From the experimental absorption spectrum, the minimum sample thickness predicted by Eq. (30) is 10.55 cm (by using the effective medium expression for  $B_e = B_0/\varphi$ ), which is only about 3 mm less than the actual sample thickness (including the acoustic sponge). It should be noted that while the ideal value of  $\varphi$  is 0.982 as mentioned previously, the actual value for the sample shown is 0.8. However, in the design of the FP channel lengths, the 0.982 value was used, and this turned out to be the most important. The lower actual value of  $\varphi$  only has the effect of reducing the reflection loss from 20 dB to 15 to 17 dB in the frequency range of 1500–3000 Hz.

As a further example to demonstrate the tunability of the absorption spectrum, we select a target spectrum as shown by the dashed line in Fig. 12, with a reflection window extending from 560 to 1000 Hz. The FP resonator length is now designed by solving Eqs. (42) and (43) with an input that is different from that for total absorption. This particular sample also has 16 FP resonators. Experimentally measured results and theory predictions by Eq. (65) are shown in Fig. 12 by open circles and solid lines, respectively. It is apparent that 16 resonators in an array are insufficient to closely mimic the target spectrum, but the resemblance is clear. In the present case the designed  $\varphi = 0.81$ , and the causal minimum thickness is 9 cm, which is 3 mm less than the actual sample thickness of 9.33 mm.

### 9. Heuristic understanding of total absorption by resonator arrays

In the experimental results presented above, the array has only 16 resonators, far from the idealized continuum model. In this

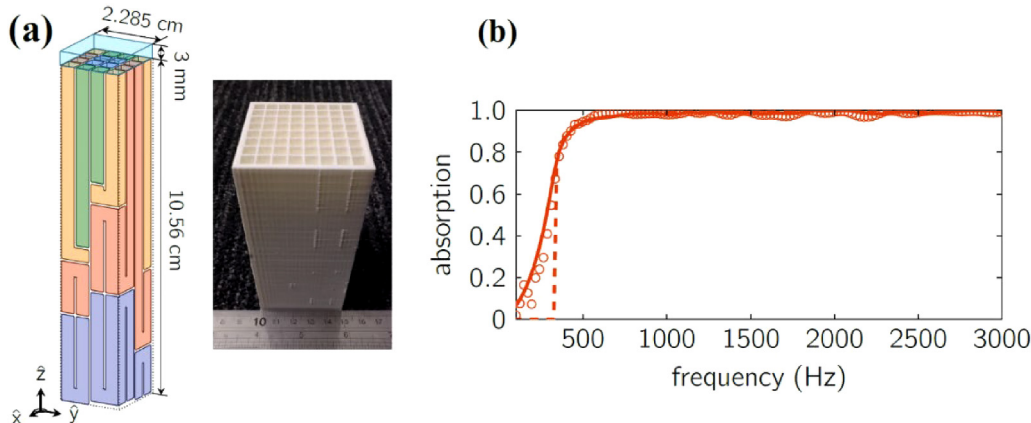


**FIG. 11.** (a) A pictorial illustration of the sample (left panel) and a photo image of the actual 3D-printed sample with four arrays. (b) Measured (shown by empty red circles) and theory (shown by black solid line) absorption spectrum of the sample shown in (a). The dashed red line indicates the target absorption spectrum used to design the sample. Deviation from the target spectrum can be attributed to the finite number (16 in the present case) of FP resonators. The sample thickness, 10.9 cm, is only ~3 mm over the causality minimum. Adapted from Ref. 15.

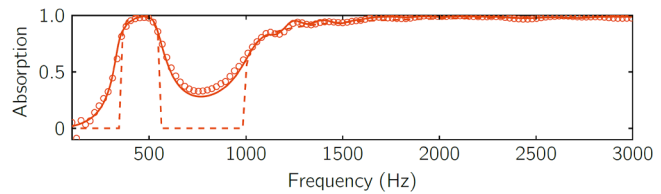


**FIG. 12.** Measured (shown by empty red circles) and theory (shown by black solid line) absorption spectrum design in accordance to the target absorption spectrum indicated by the red dashed line, using 16 FP resonators. Here the sample thickness, 9.33 cm, is only 3 mm over the causality minimum. Adapted from Ref. 15.

array, a single resonator occupies a small fraction of the total area exposed to the incident wave. It follows that at its resonance frequency, only that area fraction is absorbing. The question is: If that is the case, how can total absorption be achieved? The answer to this question can have two different aspects. In Fig. 13, we show the physical picture aspect of the answer. Similar to the flow streamline in a water sink, the Poynting vector of the incident acoustic wave energy starts to deviate from the incident wavevector at a distance above the array's surface and converges toward the resonant FP resonator. The underlying reason for this physical picture is that a discrete resonance always has high density of states to accommodate the wave energy at that frequency. Below we show the second, heuristic mathematical aspect of the answer to this question.

In accordance to Eq. (64), total absorption at the frequency of the resonator  $\tilde{n}$  is given by the condition  $Z_0^{-1} = Cf_n \text{Im}[g_n^{(e)}]$ , where  $C$  denotes some constant. The imaginary part of the Green function has a peaked shape as illustrated schematically in Fig. 14, where the red dashed line indicates the impedance matching condition for total absorption. If the frequency of the intersection point

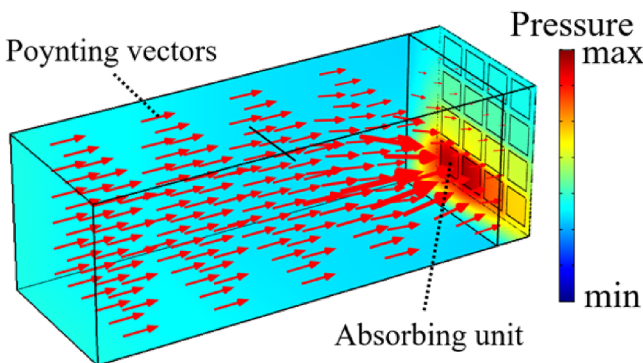


**FIG. 13.** A pictorial illustration of the Poynting vector of the incident wave at the resonance frequency of one of the resonators in the array. Close to the surface of the array, the power flow converges onto the resonating unit, leading to total absorption.

between  $C\text{Im}[g_n^{(e)}]$  and  $Z_0^{-1}$  is denoted by  $\omega_s$  as delineated by a cross, then due to the presence of the  $f_n$  factor total absorption obviously can only be achieved at another frequency  $\omega_\sigma$  indicated by an open circle, so that when the magnitude of  $C\text{Im}[g_n^{(e)}]$  at  $\omega_\sigma$  is multiplied by  $f_n$ , the result exactly meets the red dashed line. One can see that obviously if  $f_n$  is too small, i.e., the number of resonators is very large so that each occupies only a very small fraction of the total exposed area, then such a “mechanism” of frequency shift (from  $\omega_s$  to  $\omega_\sigma$ ) would not work. However, in that case the frequency difference between the resonators becomes small. Hence, when one resonator is excited by the incident wave, it is inevitable that some other resonators with resonance frequencies in the

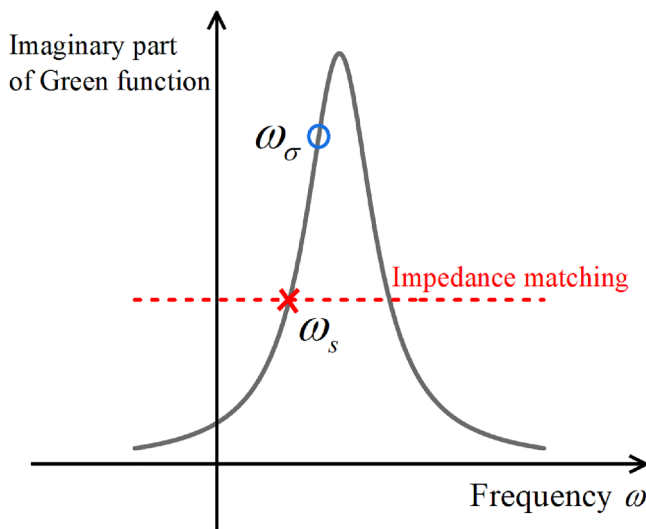


**FIG. 14.** A pictorial illustration of the slight frequency shift that can lead to the impedance matching condition as described in the text.

vicinity of the incident wave frequency will also be excited in accordance to the Lorentzian form. When that happens, total absorption at a particular frequency is no longer shouldered by a single resonator. Rather, it is achieved by a collection of resonators, each with some degree of “frequency shift.”

#### D. Further challenges in resonance-based acoustic metamaterials

Just as in any research topic, achieving broadband acoustic absorption also opens up some further challenges. Below we mention a few.

**Challenge 1:** It is easy to deduce from Eq. (30) that the absorption of air-borne acoustic waves at frequencies below 200 Hz would require sample's thicknesses that are not practical for most applications. Hence, the first challenge for resonance-based acoustic metamaterials is to find a way to circumvent the causality limitation, so as to attain near-total absorption with a sample thicknesses that can “break” the causal limit.

**Challenge 2:** Some low frequency noise is caused by machine vibrations that can reach over 120 dB. Since it is usually not possible to have an acoustic absorber with a 60 dB absorption performance, a reasonable way to remediate such problem is to first absorb the vibrational energy, so as to reduce the sound emission intensity. Vibration suppression is a well-studied field, but to absorb low frequency vibrational energy by using resonators can always be a problem, since low frequency resonators can be heavy and bulky in themselves. In this respect, a second challenge is to realize compact and light-weight low frequency resonators, with frequencies in the 10–200 Hz range that can be easily applied to suppress vibrations and maybe harvest the energy as well.

**Challenge 3:** Using resonance-based acoustic metamaterials for underwater acoustic absorption/sensing still represents a relatively un-explored area. Acoustic waves in water have wavelengths  $\sim 5$  times longer than that in air. The design of thin underwater acoustic absorbers, with a sample thickness that approaches the causality constrained limiting thickness, can represent a third challenge.

#### III. TOWARD TOPOLOGICAL ACOUSTICS AND ONE-WAY EDGE STATES

In the last section, we have been using the concept of impedance, effective density and bulk modulus to discuss absorption properties by using acoustic metamaterials, which can work in the regime where the wavelength is much larger than the lattice constant, in conjunction with resonance. On the other hand, when we go up in frequency to the diffraction regime, we have to use band structure or dispersion diagram to describe the wave properties or a structure. Special dispersion structures, such as Dirac cones, can be constructed. Taking the Dirac cone as a typical example, below we examine different ways to construct them by using accidental degeneracy or symmetry protection. These Dirac cones can occur in both the long wavelength regime as well as the diffraction regime. It allows us to have a wide range of counter-intuitive phenomena in wave manipulation, such as negative refraction, zero-index tunneling, quantum Hall-like edge states and topological bandgaps.

## A. Space-coiling structures

Acoustic metamaterials, while sharing similar concept with electromagnetic wave metamaterials, need different design strategies and realizations. In particular, for airborne acoustics, one very essential difference is that it is difficult to realize a large refractive index but easy to realize a small refractive index since sound travels much faster in any solid, fluid than in air. It is in contrary to the case of electromagnetic waves, in which index larger than that of air is easy but index smaller than air is not possible without resonance. In acoustic metamaterials, it is very usual to employ resonating structures to achieve different indices. On the other hand, inspired by how solid slows down light by a dielectric in creating multiple scatterings and phase delay, we can also create high index by delaying the sound in curled channels. Figure 15(a) shows the concept of this phase delay of sound within a curled channel across a straight-line distance  $a$ .<sup>18</sup> The factor of elongation in the path, comparing to  $a$ , is the effective refractive index  $n_{1D}$  along this direction. By assembling this curled channels into a two-dimensional network [Fig. 15(b)], it becomes the basis for constructing acoustic metamaterials with very flexibly tuned dispersion or refractive indices working both in the long wavelength and the diffraction regime, without invoking local resonances.

### 1. From negative to positive refractive indices

When the unit cells in Fig. 15(b) are assembled in a square lattice, its band structure can be solved numerically (COMSOL Multiphysics) and is plotted in Fig. 16(a). As we see from the first band, it has a much lower slope (scaled by a factor of around 5, the number of turns within each sub-unit of the curled channels) compared to the slope of the background sound line (plotted in dashed line). It means that the refractive index of such a 2D acoustic metamaterial can be easily tuned to any large value without employing any resonance. More interestingly, it will form the so-called Dirac

cones at the  $M$  point at around  $\omega a/(2\pi c) \approx 0.11$  and at the  $\Gamma$  point at around  $\omega a/(2\pi c) \approx 0.22$ . There is a very tiny bandgap opened at the center of the cone due to a small practical impedance mismatch as the Dirac cone is formed based on accidental degeneracy in this case. Anyway the dispersion is approximately linear around these Dirac cones, e.g., the cone at  $\Gamma$  point, from the band structure and this linear dispersion is isotropic near the cone center frequency, as depicted from Fig. 16(c). There is also a flatband occurring at the same frequency, which can be associated to the acoustic death band (colored green) at which the effective density is zero, to be extracted in the next section.

### 2. Effective medium extraction of wave parameters

As the dispersion returns to the  $\Gamma$  point at a low normalized frequency (wavelength in air being at least five times the size of unit cell), we expect the dispersion can also be described by an effective medium (which is also true for resonance-based metamaterials). For simplicity, rather than an analytic formulation of the detailed mechanism in creating the acoustic response, we can adopt a generic approach in extracting the effective medium parameters by using the so-called S-parameter retrieval method.<sup>19</sup> From any given set of scattering S-parameters either from full-wave simulations (such as COMSOL Multiphysics) or from an experimental measured set, the method can be used to extract effective density and bulk modulus of any acoustic metamaterials. In fact, the same can be applied to extract other constitutive parameters, such as the recently found Willis coupling parameters in analogy to electromagnetic bianisotropic constitutive parameters.<sup>20</sup>

The starting point of the method is to assume a homogeneous slab of material with density  $\rho$  and bulk modulus  $B$  (we normalize them to the values of background air for mathematical convenience here). The complex transmission coefficient  $t$  and reflection coefficient  $r$  can be easily proved by transfer matrix method to satisfy the

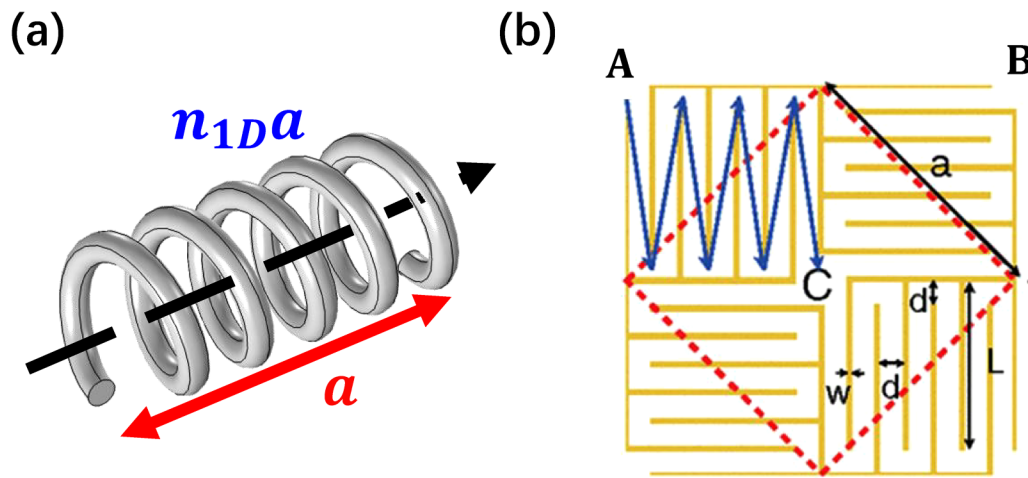


**FIG. 15.** (a) Coiling up space to allow sound to propagate within a curled channel with hard solid boundary to achieve a high refractive index  $n_{1D}$  for each channel. (b) Curled channels to form a 2D network as an acoustic metamaterial.

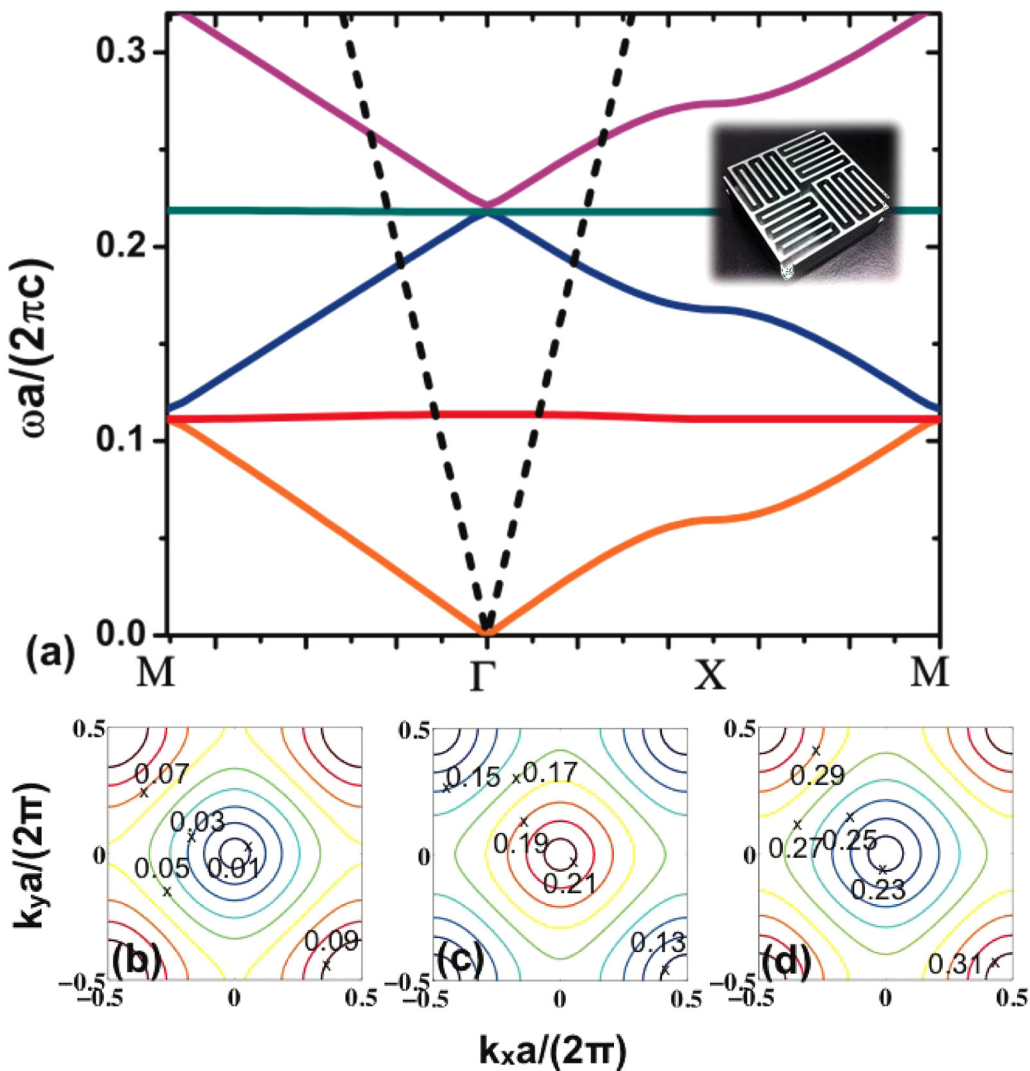


FIG. 16. (a) Band structure of a space-coiling metamaterial in square lattice (with lattice cell constant 2.33 cm for later realization) while each space-coiling unit has a 5-times folding in each channel. (b), (c), (d). Equi-frequency contour in the long wavelength limit, below, and above the Dirac cone at  $\Gamma$ -point. Adapted from Ref. 18.

following relations for a slab of thickness  $a$ :

$$i \frac{1-r-t}{1+r+t} = \frac{1}{Z} \tan\left(\frac{nk_0 a}{2}\right), \quad (66a)$$

$$i \frac{1+r-t}{1-r+t} = Z \tan\left(\frac{nk_0 a}{2}\right), \quad (66b)$$

where  $n$  and  $Z$  are the refractive index and impedance of the material, given by  $n = \sqrt{\rho} \sqrt{1/B}$  and  $Z = \sqrt{\rho} / \sqrt{1/B}$  (with normalized definition as well).  $k_0$  is the wavenumber in the background medium air. The S-parameter retrieval method basically inverts

Eq. (66) to get its solution of  $n$  and  $Z$  as

$$Z = \sqrt{\frac{1+r-t}{1-r+t}} / \sqrt{\frac{1-r-t}{1+r+t}}, \quad (67a)$$

$$nk_0 a = 2 \tan^{-1} \left( i \sqrt{\frac{1+r-t}{1-r+t}} \sqrt{\frac{1-r-t}{1+r+t}} \right), \quad (67b)$$

except that now we use the  $r$  and  $t$  from full-wave simulations with microstructures or experimental results. The inversion takes a convention in the square roots so that the real part of impedance  $Z$  is positive to satisfy the requirement of causality. There is also a

branch taking in evaluating  $\tan^{-1}$  (adding multiple integer of  $2\pi$  to  $nk_0a$  gives the same tangent value). For a thin slab, we can just take the first branch while for a thick slab, one must consider the analytic continuity when we obtain  $n$  as a function of frequency. Then, the effective  $\rho_{\text{eff}}$  and  $B_{\text{eff}}$  can be obtained as  $\rho_{\text{eff}} = nZ$ ,  $1/B_{\text{eff}} = n/Z$ . For the mentioned design of space-coiling metamaterial (with lattice constant set as  $a = 2.33$  cm), Fig. 17 shows its effective medium results from such S-parameter retrieval method being applied on either full-wave simulation results (solid lines) or experimental results (open symbols) with excellent agreement. We have plotted the real part of the refractive index  $n$ , effective density and reciprocal of effective bulk modulus in the first three panels. All of them cross the horizontal axis at a frequency around 3.12 kHz [corresponding to the normalized frequency  $\omega a/(2\pi c) = 0.22$ ], verifying the Dirac cone as indicated in Fig. 16 at this center frequency.

Through the relationship  $n = \sqrt{\rho} \sqrt{1/B}$ , the index approaches zero at the center frequency. In fact, it is called “double-zero” due to the Dirac-cone (or linear dispersion) feature. On the other hand, below the center frequency, both the density and bulk modulus become negative. In this regime, it is called the double negative metamaterial or simply negative refractive index. It becomes a value  $-1$  at around 2.7 kHz, which is usually associated with the imaging lens to do subwavelength imaging.<sup>22,23</sup>

To ensure the metamaterial to be useful for manipulating propagating waves (e.g., at the frequency having index of  $-1$ , in contrast to the previous part of this article on sound absorption), we have also extracted from the effective medium approach the imaginary part of the effective material parameters. Absorption comes from the viscosity of the air channels. More turns we curl the path, the narrower the channels become with respect to the wavelength in air, thereby inducing more contact between the sound and the solid with dissociation through the viscosity or the friction on the solid surfaces. To have an estimation on the loss, we have adopted Ref. 24 in estimating the attenuation coefficient, i.e., by adopting the form of sound amplitude  $\propto \exp(-\alpha x)$  for a straight channel along  $x$  with rectangular cross section ( $w \times h$ ), given by

$$\alpha = \left(1 + \frac{\gamma - 1}{\sqrt{Pr}}\right) \frac{w+h}{wh} \frac{1}{v_0} \sqrt{\frac{4\pi\eta f}{\rho_0}}, \quad (68)$$

where  $\rho_0$  and  $v_0$  are the density of sound speed in air,  $\eta$  is the dynamic viscosity of air and  $Pr = 0.71$  is the Prandtl number in relating the contribution of attenuation from viscosity and thermal conduction. In our case, we add an imaginary part to  $n_{1D}$ , the refractive index of a single curled channel, by  $\text{Im}(n_{1D}) = \alpha/(2k_0)$  before assembling into the 2D metamaterial with resultant effective

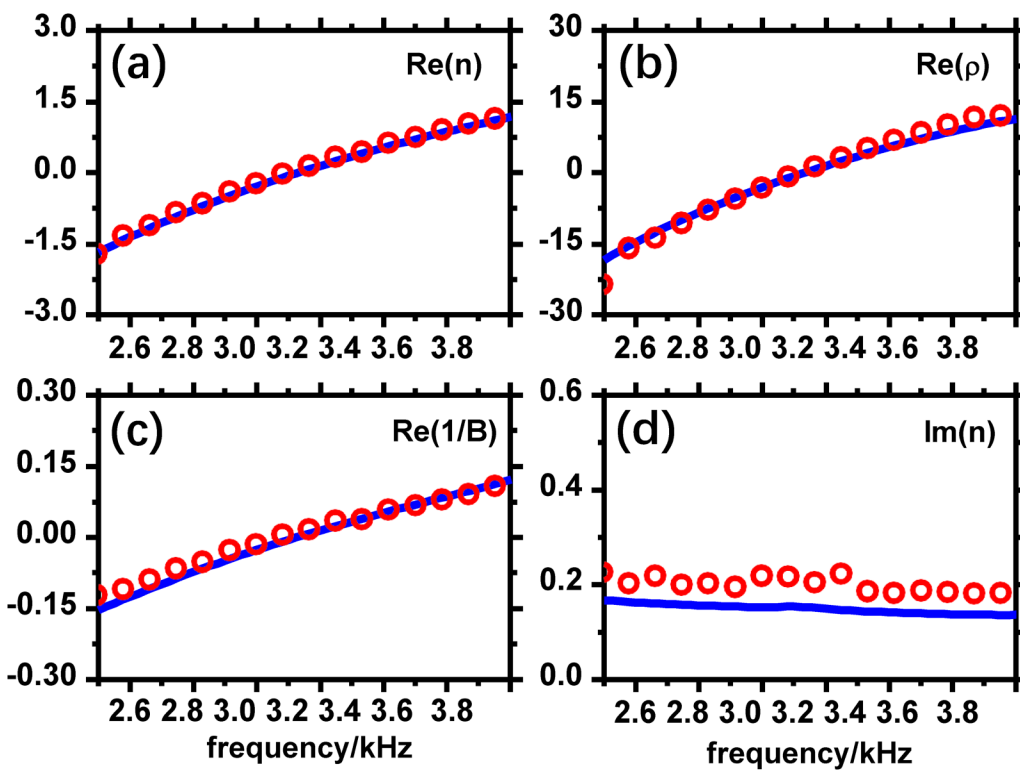


**FIG. 17.** Effective medium extracted from the space-coiling metamaterial in Fig. 16. Solid lines show the refractive index  $n$  (a), effective density (b), reciprocal of effective bulk modulus (c) and the imaginary part of the index (d). The open symbols are the corresponding results extracted from experimental data. Adapted from Ref. 21.

index  $n$ . The imaginary part of refractive index of  $n$  is found numerically to be around 20% of the real part at that frequency (agreeing with the direct measurement of attenuation for the metamaterial), which is not easy to achieve for metamaterials based on resonating mechanism for a negative refractive index. It is also worth to note on what we previously mentioned about zero density. At zero effective density, the acoustic wave equation for plane wave solution becomes simply  $\mathbf{k} \cdot \mathbf{v} = 0$ , where  $\mathbf{v}$  is the velocity field. It means that it supports transverse polarizations (rather than longitudinal) being perpendicular to the wave vector. It is the origin of the flatband at the center frequency in the band structure (Fig. 16).<sup>25</sup> This argument also implies that the band is doubly degenerate. Such a situation is well known in electromagnetic waves in which the longitudinal plasma mode exists at the frequency with zero permittivity.

### 3. Negative refraction and zero index tunneling

A direct consequence of the broadened domain of refractive index values for the acoustic metamaterial is to allow a direct demonstration of negative refraction at a negative index, as well as zero index-tunnelling at the frequency having zero refractive index (also the center frequency of the Dirac cone). Figure 18 shows a simulation to demonstrate negative refraction from a 45° right-angle prism (schematically shown in the same figure) made of unit cells with curled channels. When wave impinges on one interface at normal incidence, it enters the prism and hits another interface (metamaterial-to-air) at 45°. Then, the refractive angle  $\theta$  is governed by the Snell's law  $\sin\theta = ns\sin45^\circ$ , with  $\theta$  being positive (negative) above (below) the surface normal which is shown as a dashed straight line in the figure. The full-wave simulation results in Fig. 18(b) shows sound wave intensity measured at different angles at different frequencies. At an individual frequency, the resultant angular profile is normalized to its highest intensity, which can be defined as the refraction angle. It is obvious to note that the refraction angle varies from negative to positive in the interested frequency regime (2.6–3.8 kHz), verifying negative refraction is achieved and is associated with negative refractive indices below 3.1 kHz (the zero index frequency).

It has been pointed out and later realized (first proposed in electromagnetism and later in acoustics) that a zero refractive index<sup>26–30</sup> can be used for tunneling in a waveguide with an obstacle. This occurs at the center frequency of the Dirac cone. In Fig. 18(c), we have simulated this situation when we wrap a hard solid obstacle in such a waveguide (also with hard solid as top and bottom boundary) by 28 layers of the current acoustic metamaterial unit cells. When a wave at 3.2 kHz impinges from the left of the waveguide with an incident amplitude of 1, the wave tunnels through the waveguide with nearly unit transmittance and nearly flat wavefront. The small reflection is seen, due to the imperfect mini gap opened around the center frequency of the Dirac cone. As the Dirac cone is constructed by accidental degeneracy, any imperfections in the design due to the impedance mismatch of the channels to the background can open a tiny bandgap [with a width of ~0.2 kHz in this case, as shown in Figs. 18(b) and 18(c)].

### B. Pseudo-magnetic field and edge states

Dirac cone, a conic dispersion originally described by the Dirac equation,<sup>31</sup> has attracted great attention in electronic<sup>32,33</sup> and classical wave systems,<sup>34–38</sup> due to the associated rich physics such as one-way edge modes,<sup>35,36,39</sup> Zitterbewegung oscillations,<sup>40</sup> extremal transmissions,<sup>41,42</sup> and Klein tunneling.<sup>43</sup> Historically, the existence of Dirac cones is closely related to the crystal symmetry.<sup>44</sup> High crystal symmetry supports deterministic Dirac degeneracies at high symmetry points of the Brillouin zone (BZ). While in the case of without high enough crystal symmetry, e.g., the accidental degeneracies described in the last section, can also be generated by fine-tuning the parameters. Due to the advent of state-of-the-art fabrication technologies, the artificial crystals for classical waves can now provide a versatile platform for studying the Dirac cones and associated physical phenomena.

Inspired by recent works<sup>45–52</sup> in distorting the underlying lattice in supporting the Dirac cones (originally considered in the context of strained graphene), pseudo-magnetic field can be generated and it provides new ways to manipulate wave and ray trajectories. The concept of a pseudo-magnetic field comes from the analogy to Lorentz force acting on an electron, which consists of a conservative part due to the electric potential and electric field, and a non-conservative part associated with the magnetic field. In acoustics or any other scalar waves, the similar concept can be formulated by modifying the harmonic wave equation (in two dimensions for simplicity) as

$$(\nabla + ik_0\mathbf{A}) \cdot \frac{1}{n}(\nabla + ik_0\mathbf{A})p + k_0^2np = 0. \quad (69)$$

Compared to the usual Helmholtz wave equation, a fictitious 2D real vector  $\mathbf{A} = A_x\hat{x} + A_y\hat{y}$  is introduced into the wave equation. While its realization is described in the next section, its meaning is intuitive in terms of ray dynamics, which can be considered by writing down the Hamiltonian, or dispersion relationship, as

$$\mathcal{H}(\mathbf{k}, \mathbf{r}) = \frac{1}{2k_0n}(|\mathbf{k} + k_0\mathbf{A}|^2 - k_0^2n^2) = 0. \quad (70)$$

Then, the ray position ( $\mathbf{r}$ ) as the rate change of path length  $s$  is governed by Hamilton's equations

$$\frac{d\mathbf{r}}{ds} = \frac{\partial \mathcal{H}}{\partial \mathbf{k}} = \frac{\mathbf{k} + k_0\mathbf{A}}{k_0n}, \quad (71a)$$

$$\frac{d\mathbf{k}}{ds} = -\frac{\partial \mathcal{H}}{\partial \mathbf{r}} = \frac{|\mathbf{k} + k_0\mathbf{A}|^2 + k_0^2n^2}{2k_0n^2}\nabla n - k_0(\nabla \mathbf{A}) \cdot \frac{d\mathbf{r}}{ds}, \quad (71b)$$

which implies the ray equation

$$\frac{d}{ds} \left( n \frac{d\mathbf{r}}{ds} \right) = \nabla n - \hat{s} \times \nabla \times \mathbf{A}. \quad (72)$$

Equation (72) can be regarded as Newton's second law for ray dynamics, with the right-hand side being the Lorentz force acting on electronic motion.<sup>53</sup> The first term is conservative, where the

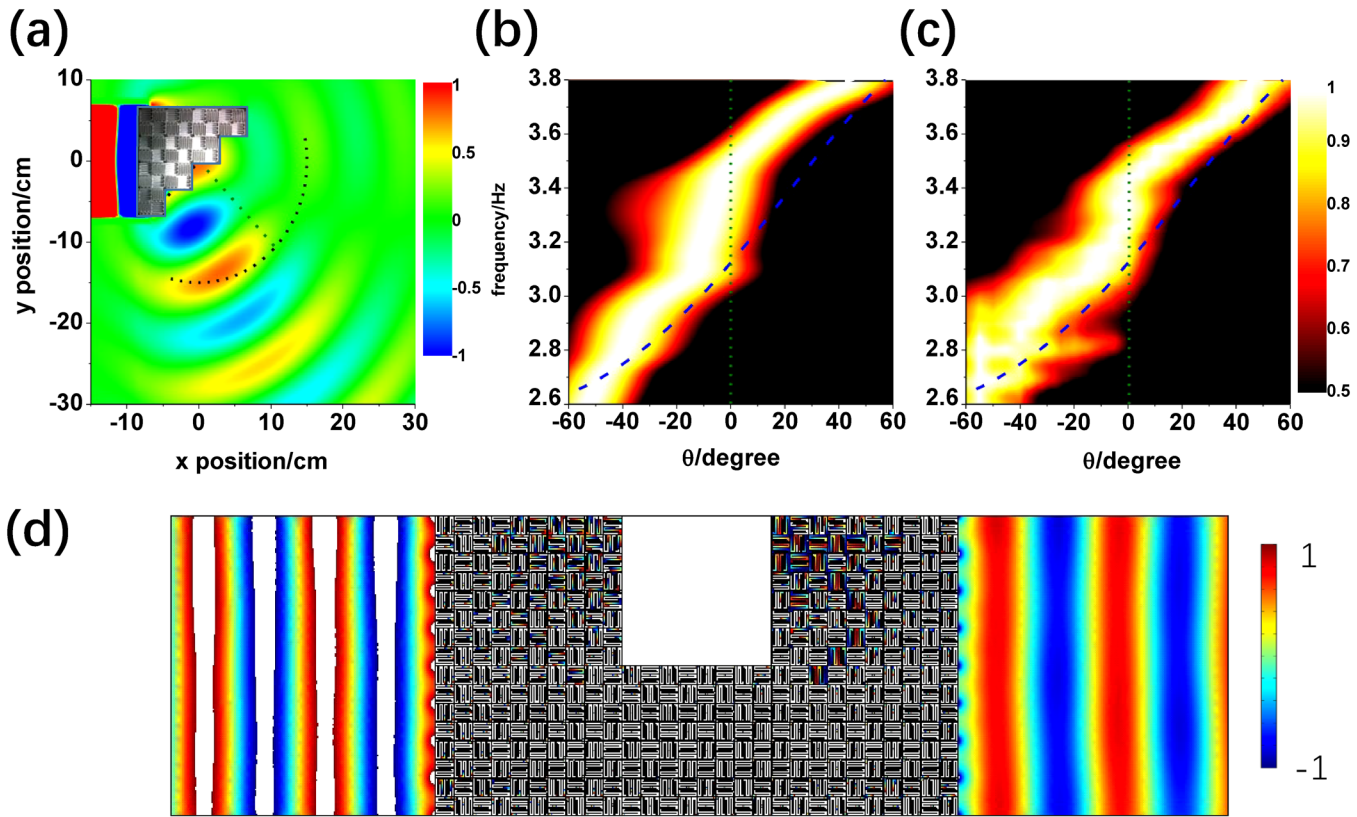


**FIG. 18.** (a) Simulated negative refraction for a prism made of space-coiling metamaterial. Outgoing beam below/above the dashed straight line indicates negative/positive refraction angle. (b) Simulation results of refraction angle  $\theta$  for an impinging wave normally hitting on one interface of the prism across different frequencies. Negative refraction ( $\theta < 0$ ) is found below 3 kHz. (c) Experimental results verifying negative-to-positive refraction across the zero-index frequency. (d) zero index tunnelling around an obstacle made of hard solid (white region). Adapted from Refs. 18 and 21.

index corresponds to the scalar potential, and  $\nabla n$  corresponds to the electric field. The second term, as a “force” perpendicular to the ray direction  $\hat{s}$ , can be regarded as the magnetic force, where  $A$  corresponds to the vector potential, also denoted as the gauge field, and  $\nabla \times A$  corresponds to the magnetic field. It makes sense to define a pseudo-magnetic field as

$$\mathbf{B} = B\hat{z} = \nabla \times \mathbf{A}. \quad (73)$$

The immediate impact of the pseudo-magnetic field, in correspondence to the magnetic force acting on an electron, is the analogy of cyclotron motion. Suppose we consider a constant pseudo-magnetic field  $B$  within a circular region  $r \leq r_0$ . To simulate the propagation of a beam with pseudo-magnetic field with Eq. (69), we impose a spatial profile of gauge field  $A$  as

$$\mathbf{A} = \begin{cases} \frac{r}{2} B \hat{\phi}, & r \leq r_0, \\ \frac{r_0^2}{2r} B \hat{\phi}, & r > r_0. \end{cases} \quad (74)$$

The vector potential  $A$  is not unique for a fixed profile of  $B$ , as also suggested by its name “gauge” field. The gauge can be fixed, e.g., by the Coulomb gauge ( $\nabla \cdot A = 0$ ). Figure 18(a) shows a beam propagating in such a region, which is bent in the counterclockwise direction in a circular motion. When the sign of  $B$  flips, the bending direction will change to clockwise. When the magnitude of  $B$  increases, the radius of the circular motion decreases. Due to the preferential bending direction within the region of non-zero  $B$  field, the  $B$ -field profile can be arranged into a setting with opposite sign on the opposite sides of an interface. In such a case, the ray is localized on such interface by the bending mechanism. This is shown in full-wave simulation for this localized state propagates from the left in Fig. 19(b). The red arrow shows the ray trajectories in bending along the interface. Even though such a localized state encounter a corner of the interface, it still bends around it and goes forward. As the bending mechanism is not compatible with propagation in the reverse direction, reflection of such state around the corner is forbidden. That is, if we imagine the ray trajectory of such a state is in the reverse direction, it would require clockwise (counterclockwise) bending in the lower (upper) medium, but this is not

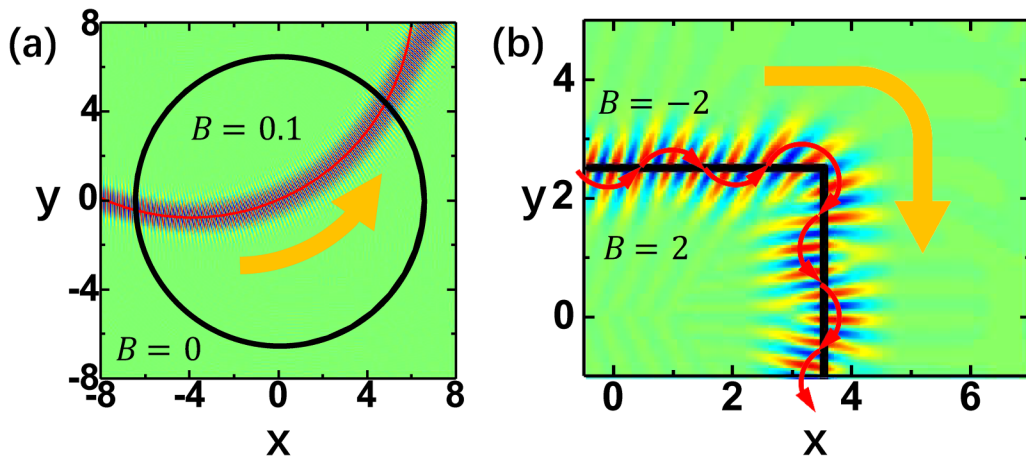


**FIG. 19.** (a) a beam propagating with constant pseudo magnetic field  $B = 0.1$  within a circular region of radius 6.5.(b) a one-way edge state propagating along a corner with  $B = 2$  ( $-2$ ) on the inner (outer) region.

the case of cyclotron motion in Fig. 19(a). Such a state is called the one-way edge mode and the same mechanism, together with the cyclotron motion, is associated with the quantum Hall effect. Unlike electron motion, the mentioned magnetic-force bending is not readily available in classical wave systems. One way to realize such pseudo-magnetic field is through the strained graphene approach.<sup>45</sup> Such a synthetic or pseudo-field approach opens the door to explore magnetic phenomena in classical wave systems but without actually employing any physical magnetic field.<sup>54–56</sup>

### 1. Shifting Dirac cones at high symmetry points

In this section, we describe how a pseudo-magnetic field, generated by the gauge field  $A$ , can be materialized. In the domain of electromagnetic waves, the gauge field  $A$  can be conceptually realized in the effective medium regime by using metamaterials with tiled anisotropy together with the concept of pseudo-spin.<sup>53</sup> The wave equation for a particular pseudo-spin becomes Eq. (69). In acoustics, we have to look for an appropriate design of phononic crystals, working in the diffraction regime, in which the dispersion surface satisfies effectively the description of Eq. (70) around a symmetry point in the Brillouin zone, and the ray dynamics will be governed by Eq. (72). In particular, we can start from a 2D phononic crystal with a triangular lattice, schematically shown in Table I. It consists of a triangular array of circular rigid cylinders in air (with radius of cylinders  $r$  being 9 mm and lattice constant  $a$  being 25 mm), carrying point group symmetry  $C_{6v}$ .<sup>57</sup> In the reciprocal space, the phononic crystal supports six Dirac cones at  $K$  or  $K'$  points in BZ. When the circular cylinders are deformed into elliptical ones, where  $p$  and  $q$  represent the semi-major and semi-minor axes, respectively, with fixed filling fraction [Fig. 20(a)], the point group symmetry is reduced to  $C_{2v}$ , which results in the shifting of Dirac points along the  $k_x$  direction, as schematically shown in Fig. 20(b). Due to the time reversal symmetry, the Dirac cones at  $K'$

points shift in opposite directions to that of Dirac cones at  $K$  points, as indicated by the blue and red arrows. Below, we focus on the Dirac cones at  $K$  points only. For elliptical deformations with  $p < q$ , these Dirac cones, originally with dispersion  $\omega - \omega_D = v_D(k_x\sigma_x + k_y\sigma_y)$  measured from the cone center  $K$  and Dirac frequency  $\omega_D = 6.97$  kHz, shift to the right by  $\delta k_x$ . Here,  $\sigma_x$  and  $\sigma_y$  are the first two Pauli matrices. On the other hand, the cones shift in the reverse direction for  $p > q$ , as shown in Fig. 20(c), numerically found to satisfy  $\delta k_x = 0.59\pi(q - p)/(pa)$ . It is worthy to mention that, the shape deformation shifts Dirac cones but hardly affects Dirac frequency  $\omega_D$ . The shifting of the Dirac cones can now be written as  $\mathbf{k} \rightarrow \mathbf{k} + \mathbf{A}$ , where  $\mathbf{A}$  is now interpreted as the gauge field (or pseudo-vector potential) and a spatially varying profile of such  $\mathbf{A}$  can be used to generate pseudo-magnetic field and edge states. Such a gauge field approach is summarized in the first row in Table I. A complementary approach to generate the edge state is to adopt the mentioned gauge field  $A$  and pseudo-magnetic field  $B$  to the reciprocal space instead of the real space. It involves opening topologically non-trivial bandgap (second row in Table I). One way to construct the appropriate phononic crystal is gapping the double Dirac cone, but its discussion will be postponed to a latter section.

### 2. Acoustic Landau levels

The linear relationship between the momentum shift and the shape factor can be used to construct a phononic crystal with a linear gauge field in the  $y$  direction. By linearly varying the shape factors of scatterers along the  $y$  direction through a relationship  $\xi(y) = -B_z y/c_\gamma$ , where  $c_\gamma = 0.59\pi/a$ , and  $\xi = (q - p)/p$  is the dimensionless shape parameter governing the elliptical cross sectional shape of the cylinders, a linearly gradient gauge field  $A_x(y) = -B_z y$  can be constructed in the phononic crystal, where the constant  $B_z$  defines the strength of acoustic pseudo-magnetic

**TABLE I.** Summarizing the approaches to realize the pseudo-magnetic field in real space and reciprocal space with a triangular lattice, corresponding to the upper and lower rows, respectively.

Unit-cell	Brillouin zone	Perturbation on unit cell	Pseudo-magnetic field	Edge modes required
 Triangular lattice	 Primitive unit cell	 Dirac cones at $K$ and $K'$	Lowering point group symmetry	In real space Spatially varying gauge field
 Extended unit cell	 Double Dirac cone at $\Gamma$	Lowering lattice symmetry	In reciprocal space	Topologically non-trivial bandgap

field orientated in the  $z$  direction. The inset in Fig. 21(a) schematically shows a gradient 91-layer ( $-45 \leq n_y \leq 45$ ) phononic crystal ribbon, which can be used to construct the 2D gradient phononic crystal by periodically arranging in the  $x$  direction. According to  $\mathbf{B} = \nabla \times \mathbf{A}$ ,  $B_z = -\frac{\partial A_x}{\partial y} = -0.013a^{-2}$  (the minus sign indicates  $-z$  direction). In analogy to electron undergoing cyclotron motion and quantization into Landau levels, the linear Dirac cones here also quantizes into a sequence of discrete acoustic Landau levels (LLs), which is clearly observed in the spectrum around the  $K$  point (set as the original point) for the 91-layer gradient ribbon in Fig. 21(b). Clearly, the spectrum exhibits discrete flat Landau plateaus centered by the Dirac frequency  $\omega_D = 6.97$  kHz,

which is the hallmark of Landau quantization for massless Dirac systems. The analytical LLs (at frequencies  $\Delta_n$  with respect to the Dirac frequency) calculated from the effective Dirac Hamiltonian  $H = v_D((P_x + A_x)\sigma_x + P_y\sigma_y)$  with  $P_{x,y}$  being the momentum operator,<sup>58</sup> which can be written as

$$\Delta_n = \text{sign}(n)\sqrt{|n|}\omega_c, \quad (75)$$

where  $\omega_c = v_D\sqrt{2|B_z|} = 200$  Hz is an acoustic analog of the cyclotron frequency, with  $v_D = \partial\omega/\partial k = 1241.4a$  being obtained from the Dirac dispersion. In Fig. 21(b), the bold lines representing analytical LLs (with the Dirac frequency as the center frequency),

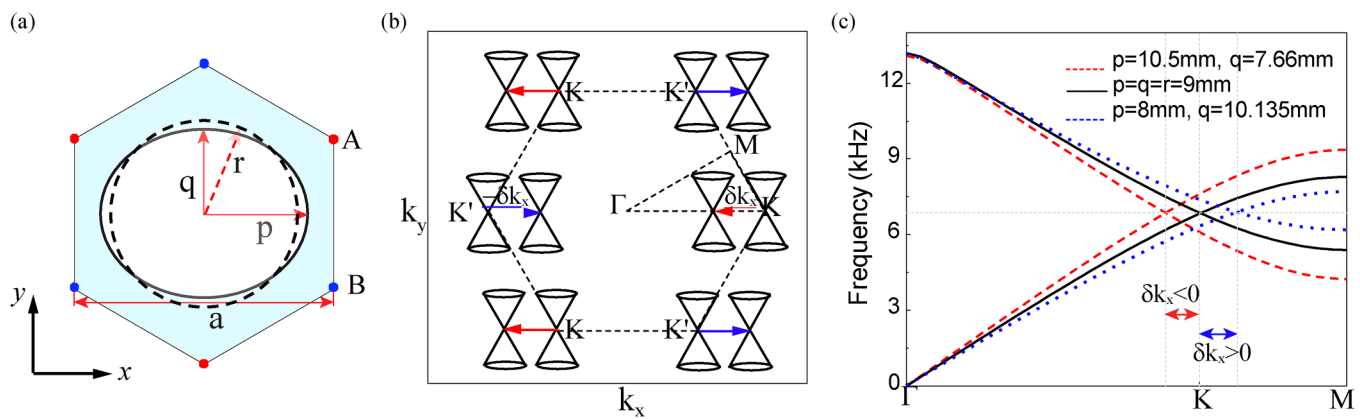


**FIG. 20.** (a) The unit-cell of the triangular phononic crystals with cylinder being deformed into an elliptical one. (b) With reduced crystal symmetry, the Dirac cones at the corner of BZ shifts along  $k_x$  direction in momentum space. (c) The band structures for three uniform phononic crystals with different shape of cylinders. The location of Dirac cone (indicated with vertical gray lines) shifts for the deformed cylinders but with almost the same Dirac frequency (indicated with horizontal gray line).

match perfectly with the simulated results for the first 11 LLs. The states in each Landau plateau are accidentally degenerated, as they share the same energy but their wave functions center at different  $y$ -coordinates. The high degeneracy in discrete LLs results in the high density of states, which will be reflected by the mode profile and excitation spectrum.

Here, we demonstrate a bulk state and two edge states in the zeroth LL for the 91-layer phononic crystal [marked with black dots in Fig. 21(b)], whose eigen-mode profiles (normalized by the largest value) are shown in Fig. 21(c). For the bulk states in Landau

plateau (middle panel), the pressure field situates at the center of the sample, and spreads over a length scale of the effective magnetic length  $l_B = 1/\sqrt{|B_z|} = 8.8a$  (marked with the black arrow). However, for the edge state in the gap between  $n = 0$  and  $n = 1$  LLs, the pressure field localizes at lower boundaries, as shown in the left panel. In contrast, the edge state in the gap between  $n = 0$  and  $n = -1$  LLs corresponds to the upper edge states, as shown in the right panel. Physically, the edge states arise from the opened acoustic cyclotron orbits (green arrow) near a ribbon edge, in contrast to the complete cyclotron orbit for the bulk states (middle

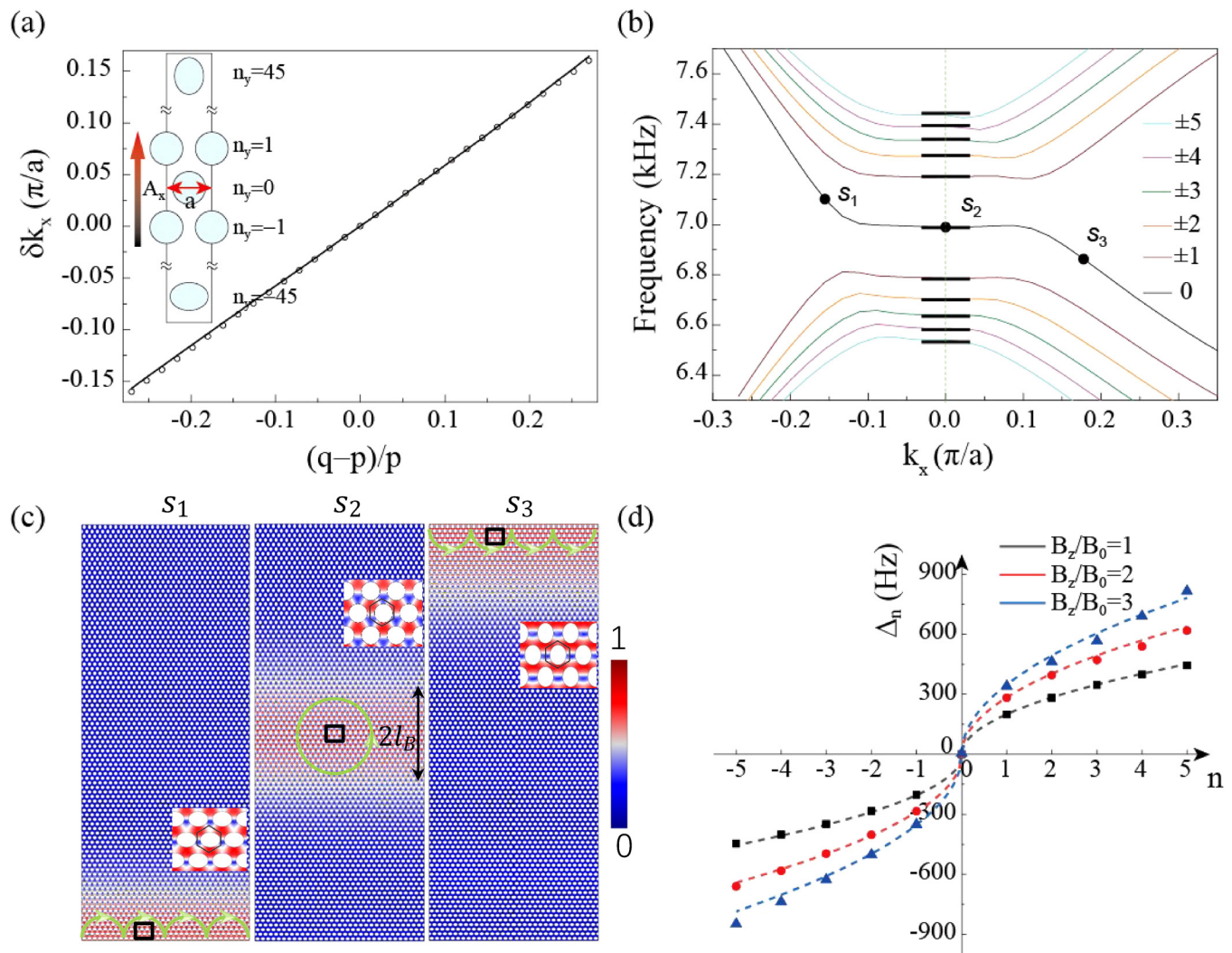


**FIG. 21.** (a) Simulated momentum shifts  $\delta k_x$  or  $A_x$  with a linear dependence (line) on the deformation shape factor  $\xi = (q - p)/p$ , which is used to construct the a linear profile of  $A_x$  in a gradient 91-layer phononic crystal consisting of a periodic array of the ribbon (inset) in  $x$  direction. (b) Landau level spectrum center around the Dirac frequency around  $K$  point, simulated for the ribbon in (a), where the bold lines represent the analytically predicted LLs. Adapted from Ref. 57. (c) The normalized pressure amplitude distributions for bulk ( $s_2$ ) and edge ( $s_1$  and  $s_3$ ) states in a gradient 91-layer phononic crystals. The direction of the trajectories of the states are schematically indicated by the green arrows. Insets: the zoom-in field pattern within the black frame. (d) The first 11 LLs for phononic crystals with different magnetic strength  $B_z$  (achieved by adjusting the number of layers in phononic crystal), where the symbols and dashed lines represent the simulated and analytical results respectively.

panel). For edge states, the frequencies deviate gradually from the LL values, as these states become more and more localized at the edge. In addition, the bulk-state vibrations behave strikingly different at the two sublattices: the field concentrates around the A sublattice but vanishes at the B sublattice, as the inset shows. This is a direct consequence of the graphene-like Dirac systems, where the zeroth LL states are sublattice polarized (the eigenvector for the zeroth LL obtained from the effective Hamiltonian is zero for B sublattice), in contrast to the states in other LLs that occupy both sublattices. The polarization weakens as the state departs from the Landau plateau due to the interaction with the physical boundary (see insets).

For the phononic crystal with macroscopic controllability, it is easy to achieve stronger uniform pseudo-magnetic field. With  $A_x(y) = -B_z y$ , for example, we can simply decrease the number of layers, that is, decrease  $y$  to increase the gradient to achieve stronger pseudo-magnetic field as exemplified in Fig. 21(d). Here, we take  $B_z = -0.013a^{-2}$  achieved in the 91-layer gradient phononic crystal as the baseline  $B_0$ . By decreasing the number of layers of the gradient phononic crystal to 46 layers and 31 layers, we can achieve the double ( $B_z/B_0 = 2$ ) and triple value ( $B_z/B_0 = 3$ ). The symbols represent the simulated results for the first 11 LLs ( $|n| \leq 5$ ), and consistent with the analytical results obtained from Eq. (75) (dashed lines), even for stronger pseudo-magnetic field. In addition, the Dirac LLs in phononic crystals show a square-root dependence on the pseudo-magnetic field, in contrast to the equally spaced LLs with a linearly dependence on magnetic field for free 2D electrons in a real magnetic field.

### 3. Experimental realization

As high degeneracy in discrete LLs leads directly to high density of states, we can experimentally observe the quantized

acoustic LLs through the peak structure of the excitation spectrum. To facilitate the experimental demonstration of the quantized acoustic LLs well separated in the frequency spectrum (larger separations between different  $\Delta_n$ ), a higher pseudo-magnetic field  $B_z$  is preferred according to Eq. (75). In our case, the pseudo-magnetic field is constructed from a linear gradient of  $A_x$  ( $\delta k_x$  of the Dirac cones) in the y-direction, which in turns comes from the deformation of the unit cells across the whole phononic crystal, described in Fig. 21(a). Therefore, we further decrease the number of layers from 91 to 16 layers, corresponding to a six-fold increase of the pseudo-magnetic field of the theory simulation in Fig. 21 ( $B_z = -0.078a^{-2}$ ) to achieve separations of the LLs. The experimental setup is shown in Fig. 22(a). Due to the sublattice polarization nature of the zeroth LL state, the location of the sound source (A-sublattice or B-sublattice) can profoundly affect the excitation spectrum. For comparison, a point-like sound source is placed at one A-sublattice and one B-sublattice near the sample center for excitation, and the measured frequency spectra for the total sound energy are plotted as red and blue circles in Fig. 22(b), respectively, and the red and blue solid lines represent the respective simulated results. For the A-site spectrum (red), three discrete peaks corresponding to the first three LLs are clearly observed, dramatically different from the quadratic background spectrum (black dashed line) simulated for a 16-layer sample with zero pseudo-magnetic field. Specifically, the primary peak, corresponding to the zeroth LL, is a key feature of the Landau quantization in a relativistic Dirac system. However, for B-site excitation spectrum (blue), the zeroth LL cannot be excited effectively because the zeroth LL lives entirely on the A-sublattice [as shown in the inset of Fig. 21(c)], while the  $n = -1$  and  $n = 1$  LLs without sublattice polarization can be excited by B-site excitation. The quantization peak locations

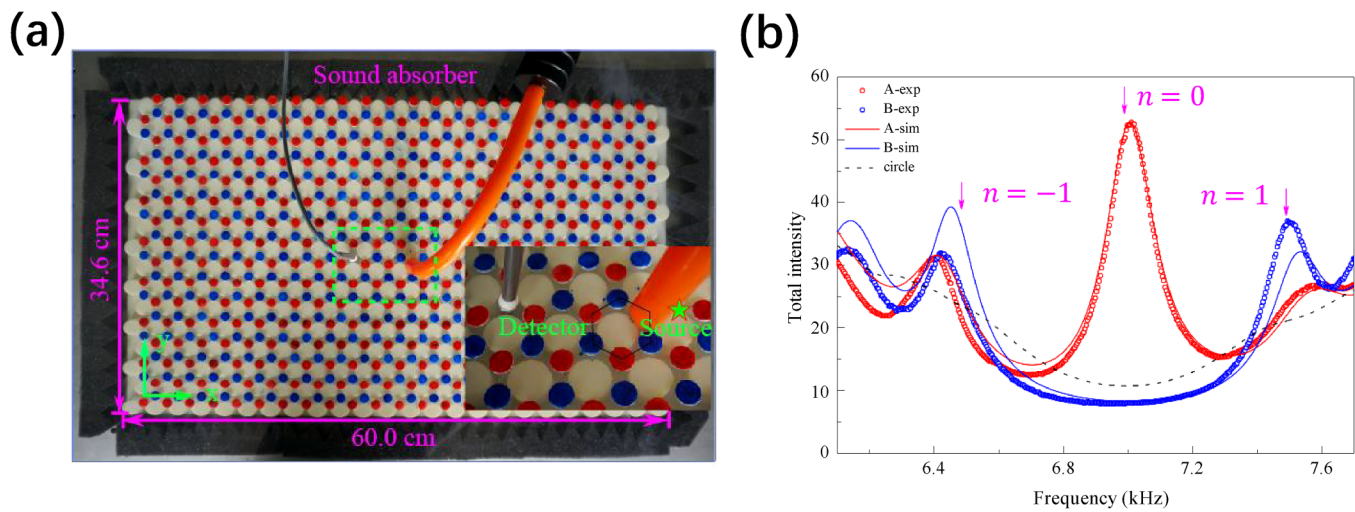


**FIG. 22.** (a) The experimental setup, a 16-layer 2D phononic crystal is covered by a transparent holey plate to form a 2D acoustic waveguide for measurement. The preserved holes are sealed by plugs colored in red and blue respectively for A and B sublattices of each unit-cell [as shown in Fig. 19(a)], will be opened one-by-one for sound detection, where the inset shows a zoom-in image indicating the sound source and detector. (b) The frequency spectra of the total intensity for A and B sublattice excitation are plotted with red and blue open circles respectively, agrees well with the numerical results (solid lines), whose peak structures follow the model prediction (purple arrows). Adapted from Ref. 57.

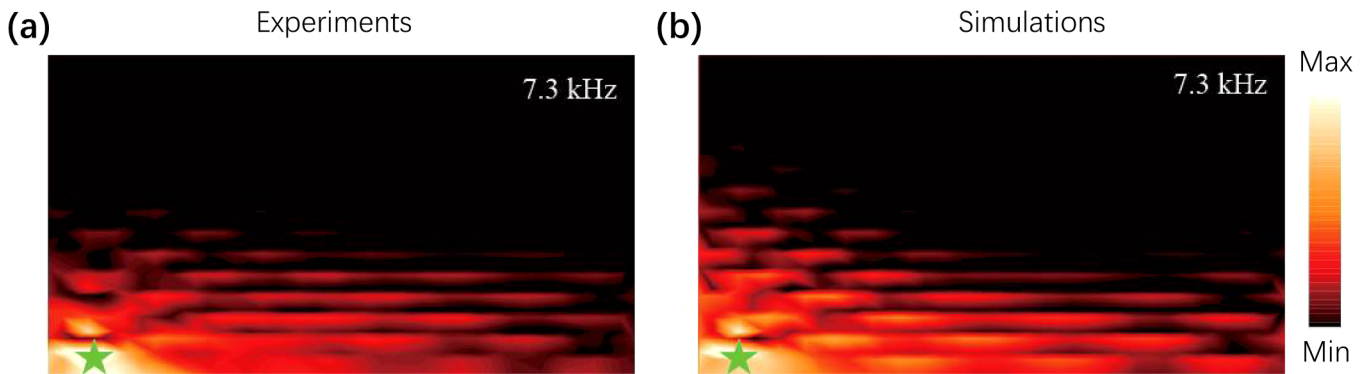


**FIG. 23.** (a) Measured field pattern for a bottom edge state in a 16-layer phononic crystal with a strong pseudo magnetic field. (b) Simulated field pattern from Comsol Multiphysics. Adapted from Ref. 57.

in the excitation spectra that result from the acoustic pseudo-magnetic field, match well with the expected positions (indicated with purple arrows) calculated by Eq. (75).

In addition to the above, we can observe the quantum-hall-like edge modes in the gaps between two neighboring acoustic LLs by using a similar experimental setup shown in Fig. 22(a) but with rigid strips attached at the upper and lower boundaries to prevent sound leakage. Here, we exemplify the measurement of edge states localized at the bottom boundary with a frequency at 7.3 kHz, which falls into the gap between  $n = 0$  and  $n = 1$  LLs. For the observation of edge states that propagate along the bottom boundary, a sound source (green star) is positioned at the bottom left of the sample to excite the edge mode that travels to the right direction. The measured pressure distributions for bottom edge states is shown in Fig. 23(a), a well-confined edge state appears in the bottom boundary and propagates rightwards, consistent with the simulation results in Fig. 23(b). Similarly, the rightward-propagating upper edge states which falls into the gap between the  $n = 0$  and  $n = -1$  LLs can also be measured with an excitation source located at the upper left of the sample (not shown).

#### 4. Topologically non-trivial bandgap and topological edge states

Another approach to generate edge states is through a topological non-trivial bandgap. In this approach, the concepts about the gauge field and pseudo-magnetic field are directly related to the Berry connection  $A(k)$  and Berry curvature  $\Omega(k)$  in the reciprocal space, respectively. The non-zero Berry curvature  $\Omega(k)$  in the reciprocal space gives rise to topological properties of the bands. In turns, a topological edge state can be generated within a topologically non-trivial bandgap from the Dirac cone as the result. As a typical example, we start from the same triangular lattice, except that we now purposely use an extended unit-cell (rather than the original primitive one) with a lattice constant  $a' = \sqrt{3}a$ . Then, the corresponding Brillouin zone is reduced. From band folding, a double Dirac cone appears at the  $\Gamma$  point, as shown in the second row in Table I and the relevant band structure is shown in Fig. 24(b). Such an approach has been used to generate double Dirac cones for both the electromagnetic and acoustic waves and the consideration of topological nontrivial bandgap.<sup>59–63</sup> Here, we lower the lattice symmetry by introducing a perturbation only in the central

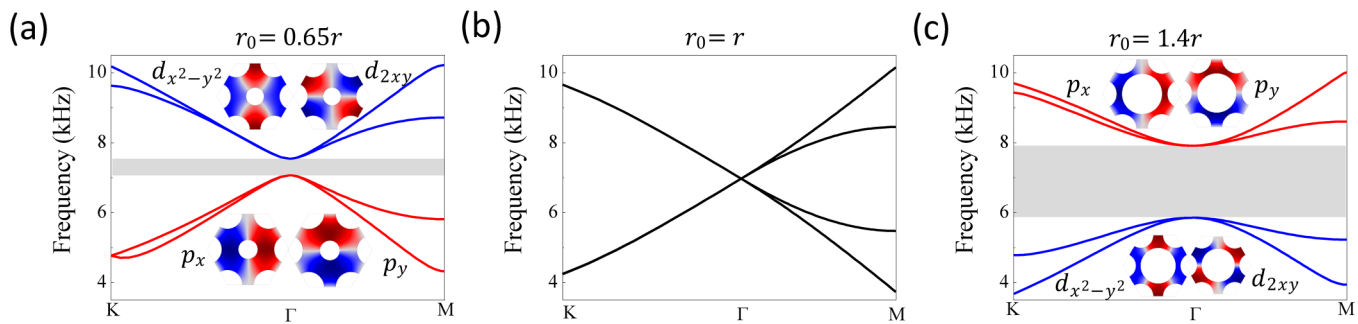


**FIG. 24.** Band structures for three phononic crystals with different radius  $r_0$  of the central cylinder. (b) With  $r_0 = r$ , the lattice symmetry allows zone folding to achieve a doubly degenerated Dirac cone at  $\Gamma$  point. With a reduced (a) or enlarged radius  $r_0$ (c), the lattice symmetry lowers and a band gap (indicated by gray regions) opens at  $\Gamma$  point. The insets show the pressure field distribution for four modes at  $\Gamma$  point.

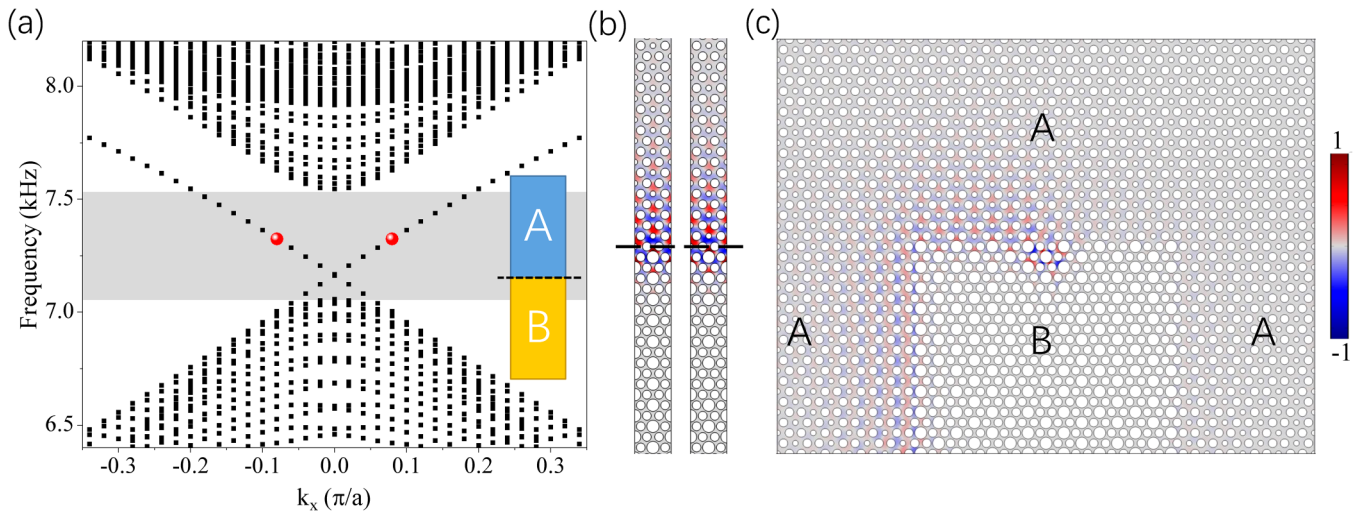


**FIG. 25.** (a) Simulated band structure for a ribbon consisting of two phononic crystals with distinct topological phase (A-B type supercell shown in the inset). Topological edge states appear at the band gap (gray region). (b) The pressure field pattern for the edge state indicated by the red dots at 7.32 kHz. (c) Topological edge state at 7.24 kHz in circulating the interface in counter-clockwise direction.

cylinder in the extended unit cell. By adjusting the radius  $r_0$  of the central cylinder to deviate from the original radius  $r$ , the original translational symmetry is broken (lowered), thereby a bandgap can be opened and tailored flexibly at the Dirac cone. For a reduced radius ( $r_0 = 0.65r$ ) in Fig. 24(a), the bandgap opens and two twofold degenerated modes are located on the upper and lower sides of the bandgap. The inset shows the pressure field patterns for the modes at  $\Gamma$  point, which can be classified into the  $p_x/p_y$  (lower two modes) and  $d_{x^2-y^2}/d_{2xy}$  (upper two modes) by following the convention in topological photonics.<sup>59,60</sup> In contrast, for an enlarged radius ( $r_0 = 1.4r$ ) in Fig. 24(c), the frequency of  $p_x/p_y$  modes is higher than that of  $d_{x^2-y^2}/d_{2xy}$  modes, which characterizes the band inversion and topological phase transition. Consequently, by adjusting the radius  $r_0$ , we achieve two topologically distinct phases. To understand such topological non-trivial bandgap, it is intuitive to adopt a spring-mass model in the hexagonal lattice.<sup>64</sup> The waves of pseudo-spin up state, defined by  $p_x + ip_y$  and  $d_{x^2-y^2} + i d_{2xy}$ , are approximately decoupled near the zone center from those of pseudo-spin down defined by  $p_x - ip_y$  and  $d_{x^2-y^2} - i d_{2xy}$ . The corresponding Hamiltonian near the bandgap can be written in the form of

$$H_{\text{eff}} = \begin{pmatrix} M + Bk^2 & A(k_x + ik_y) \\ A^*(k_x - ik_y) & -M - Bk^2 \end{pmatrix}, \quad (76)$$

which gives you the quality of the bandgap (and eigenmodes) near zone center in Fig. 24(a) (with  $BM > 0$  for the trivial case) and Fig. 24(c) (with  $BM < 0$  for the non-trivial case). It shares similar features with the Hamiltonian of the quantum spin Hall effect.<sup>59,61</sup>

Combining two phononic crystals with different topologically distinct phases, we construct an A-B type supercell ribbon, as schematically shown in the inset of Fig. 25(a). As a result, a pair of

topological edge states appear at the bulk bandgap (gray region), as shown in the band structure of the supercell in Fig. 25(a). In Fig. 25(b), we demonstrate the pressure field distribution of two topological edge states [marked with red dots in Fig. 25(a)] with a frequency at 7.32 kHz, which is localized at the interface and decay quickly along the normal direction of the interface. In Fig. 25(c), we have simulated the edge state running along on an interface when B is enclosed by A. A point-type source is excited in the middle on the interface to excite with only one single spin edge state which goes around the corner in the counterclockwise direction almost without reflection.

While the acoustic properties of the metamaterials in this article on absorption and topological acoustics are mainly driven by resonating physical structures, it is worthwhile to note that there is recently a direction in constructing acoustic metamaterials based on interconnected loudspeakers and microphones, or piezoelectric transducers with external feedback circuits, to give rise to more arbitrarily defined response of the acoustic metamaterials.<sup>65-67</sup> It allows us to have more flexibility to explore material loss (and also gain) in non-Hermitian or topological metamaterials and also allows us to have dynamical tunability and time-varying metamaterials.<sup>68-71</sup>

## ACKNOWLEDGMENTS

P.S. would like to thank Sichao Qu for help with the figures. We would also like to thank Yan Meng for his helpful discussion when the article was prepared. This work is supported by RGC grant (No. AoE/P-02/12).

## DATA AVAILABILITY

The data that support the findings of this study are available within the article.

## REFERENCES

- <sup>1</sup>Z. Liu, X. Zhang, Y. Mao, Y. Y. Zhu, Z. Yang, C. T. Chan, and P. Sheng, "Locally resonant sonic materials," *Science* **289**, 1734–1736 (2000). It should be noted that in this initial publication, the novel effect was mis-attributed to the negative modulus rather than to the dynamic mass dispersion. It was subsequently corrected in Refs. 2 and 3.
- <sup>2</sup>P. Sheng, X. X. Zhang, Z. Liu, and C. T. Chan, "Locally resonant sonic materials," *Phys. B: Condens. Matter* **338**, 201–205 (2003).
- <sup>3</sup>Z. Liu, C. T. Chan, and P. Sheng, "Analytic model of phononic crystals with local resonances," *Phys. Rev. B* **71**, 014103 (2005).
- <sup>4</sup>L. Sun, K. Y. Au-Yeung, M. Yang, S. T. Tang, Z. Yang, and P. Sheng, "Membrane-type resonator as an effective miniaturized tuned vibration mass damper," *AIP Adv.* **6**, 085212 (2016).
- <sup>5</sup>N. Fang, D. Xi, J. Xu, M. Ambati, W. Srituravanich, C. Sun, and X. Zhang, "Ultrasonic metamaterials with negative modulus," *Nat. Mater.* **5**, 452–456 (2006).
- <sup>6</sup>Z. Yang, J. Mei, M. Yang, N. H. Chan, and P. Sheng, "Membrane-type acoustic metamaterial with negative dynamic mass," *Phys. Rev. Lett.* **101**, 204301 (2008).
- <sup>7</sup>S. H. Lee, C. M. Park, Y. M. Seo, Z. G. Wang, and C. K. Kim, "Acoustic metamaterial with negative density," *Phys. Lett. A* **373**, 4464–4469 (2009).
- <sup>8</sup>P. Sheng, J. Mei, Z. Liu, and W. Wen, "Dynamic mass density and acoustic metamaterials," *Phys. B: Condens. Matter* **394**, 256–261 (2007).
- <sup>9</sup>J. Mei, Z. Liu, W. Wen, and P. Sheng, "Effective dynamic mass density of composites," *Phys. Rev. B* **76**, 134205 (2007).
- <sup>10</sup>D.-Y. Maa, "Potential of microperforated panel absorber," *J. Acoust. Soc. Am.* **104**, 2861–2866 (1998).
- <sup>11</sup>J. Mei, G. Ma, M. Yang, Z. Yang, W. Wen, and P. Sheng, "Dark acoustic metamaterials as super absorber for low-frequency sound," *Nat. Commun.* **3**, 756 (2012).
- <sup>12</sup>M. Yang, Y. Li, C. Meng, C. Fu, J. Mei, Z. Yang, and P. Sheng, "Sound absorption by subwavelength membrane structures: A geometric perspective," *Comp. Rend. Mécanique* **343**, 635–644 (2015).
- <sup>13</sup>G. Ma, M. Yang, S. Xiao, Z. Yang, and P. Sheng, "Acoustic metasurface with hybrid resonances," *Nat. Mater.* **13**, 873–878 (2014).
- <sup>14</sup>M. Yang, S. Chen, C. Fu, and P. Sheng, "Optimal sound-absorbing structures," *Mater. Horiz.* **4**, 673–680 (2017).
- <sup>15</sup>M. Yang and P. Sheng, "An integration strategy for acoustic metamaterials to achieve absorption by design," *Appl. Sci.* **8**, 1247 (2018).
- <sup>16</sup>M. Yang and P. Sheng, "Sound absorption structures: From porous media to acoustic metamaterials," *Annu. Rev. Mater. Res.* **47**, 83–114 (2017).
- <sup>17</sup>G. C. Ma and P. Sheng, "Acoustic metamaterials: From local resonances to broad horizons," *Sci. Adv.* **2**, 83–114 (2016).
- <sup>18</sup>Z. Liang and J. Li, "Extreme acoustic metamaterial by coiling up space," *Phys. Rev. Lett.* **108**, 114301 (2012).
- <sup>19</sup>D. R. Smith, S. Schultz, P. Markoš, and C. M. Soukoulis, "Determination of effective permittivity and permeability of metamaterials from reflection and transmission coefficients," *Phys. Rev. B* **65**, 195104 (2002).
- <sup>20</sup>Y. Liu, Z. Liang, J. Zhu, L. Xia, O. Mondain-Monval, T. Brunet, A. Alù, and J. Li, "Willis metamaterial on a structured beam," *Phys. Rev. X* **9**, 011040 (2019).
- <sup>21</sup>Z. Liang, T. Feng, S. Lok, F. Liu, K. B. Ng, C. H. Chan, J. Wang, S. Han, S. Lee, and J. Li, "Space-coiling metamaterials with double negativity and conical dispersion," *Sci. Rep.* **3**, 1–6 (2013).
- <sup>22</sup>J. B. Pendry, "Negative refraction makes a perfect lens," *Phys. Rev. Lett.* **85**, 3966 (2000).
- <sup>23</sup>S. Zhang, L. Yin, and N. Fang, "Focusing ultrasound with an acoustic metamaterial network," *Phys. Rev. Lett.* **102**, 194301 (2009).
- <sup>24</sup>L. E. Kinsler, R. A. Frey, A. B. Coppens, and J. V. Sanders, *Fundamentals of Acoustics* (Wiley, New York, 1999).
- <sup>25</sup>I. E. Psarobas, A. Modinos, R. Sainidou, and N. Stefanou, "Acoustic properties of colloidal crystals," *Phys. Rev. B* **65**, 064307 (2002).
- <sup>26</sup>M. Silveirinha and N. Engheta, "Tunneling of electromagnetic energy through subwavelength channels and bends using  $\epsilon$ -near-zero materials," *Phys. Rev. Lett.* **97**, 157403 (2006).
- <sup>27</sup>B. Edwards, A. Alù, M. E. Young, M. Silveirinha, and N. Engheta, "Experimental verification of epsilon-near-zero metamaterial coupling and energy squeezing using a microwave waveguide," *Phys. Rev. Lett.* **100**, 033903 (2008).
- <sup>28</sup>I. Liberal, M. Lobet, Y. Li, and N. Engheta, "Near-zero-index media as electromagnetic ideal fluids," *Proc. Natl. Acad. Sci. U.S.A.* **117**, 24050–24054 (2020).
- <sup>29</sup>F. Liu, X. Huang, and C. T. Chan, "Dirac cones at  $k = 0$  in acoustic crystals and zero refractive index acoustic materials," *Appl. Phys. Lett.* **100**, 071911 (2012).
- <sup>30</sup>C. Xu, G. Ma, Z.-G. Chen, J. Luo, J. Shi, Y. Lai, and Y. Wu, "Three-dimensional acoustic double-zero-index medium with a fourfold degenerate Dirac-like point," *Phys. Rev. Lett.* **124**, 074501 (2020).
- <sup>31</sup>J. D. Bjorken and S. D. Drell, *Relativistic Quantum Mechanics* (McGraw-Hill, New York, 1964).
- <sup>32</sup>H. Zhang, C.-X. Liu, X.-L. Qi, X. Dai, Z. Fang, and S.-C. Zhang, "Topological insulators in Bi<sub>2</sub>Se<sub>3</sub>, Bi<sub>2</sub>Te<sub>3</sub> and Sb<sub>2</sub>Te<sub>3</sub> with a single dirac cone on the surface," *Nat. Phys.* **5**, 438–442 (2009).
- <sup>33</sup>S. Q. Shen, *Topological Insulators* (Springer, Berlin, 2012), Vol. 174.
- <sup>34</sup>L. Lu, J. D. Joannopoulos, and M. Soljačić, "Topological photonics," *Nat. Photon.* **8**, 821–829 (2014).
- <sup>35</sup>Z. Yang, F. Gao, X. Shi, X. Lin, Z. Gao, Y. Chong, and B. Zhang, "Topological acoustics," *Phys. Rev. Lett.* **114**, 114301 (2015).
- <sup>36</sup>J. Lu, C. Qiu, L. Ye, X. Fan, M. Ke, F. Zhang, and Z. Liu, "Observation of topological valley transport of sound in sonic crystals," *Nat. Phys.* **13**, 369–374 (2017).
- <sup>37</sup>J. Lu, C. Qiu, M. Ke, and Z. Liu, "Valley vortex states in sonic crystals," *Phys. Rev. Lett.* **116**, 093901 (2016).
- <sup>38</sup>S.-Y. Yu, C. He, Z. Wang *et al.*, "Elastic pseudospin transport for integrable topological phononic circuits," *Nat. Commun.* **9**, 3072 (2018).
- <sup>39</sup>Y. Poo, R. Wu, Z. Lin, Y. Yang, and C. T. Chan, "Experimental realization of self-guiding unidirectional electromagnetic edge states," *Phys. Rev. Lett.* **106**, 093903 (2011).
- <sup>40</sup>X. Zhang, "Observing zitterbewegung for photons near the Dirac point of a two-dimensional photonic crystal," *Phys. Rev. Lett.* **100**, 113903 (2008).
- <sup>41</sup>R. A. Sepkhanov, Y. B. Bazaliy, and C. W. J. Beenakker, "Extremal transmission at the dirac point of a photonic band structure," *Phys. Rev. A* **75**, 063813 (2007).
- <sup>42</sup>X. Zhang and Z. Liu, "Extremal transmission and beating effect of acoustic waves in two-dimensional sonic crystals," *Phys. Rev. Lett.* **101**, 264303 (2008).
- <sup>43</sup>C. Shi, Z. Li, X. Li, S. Wang, Y. Wang *et al.*, "Direct observation of Klein tunneling in phononic crystals," *Science* **370**, 1447–1450 (2020).
- <sup>44</sup>J. Lu, C. Qiu, S. Xu, Y. Ye, M. Ke, and Z. Liu, "Dirac cones in two-dimensional artificial crystals for classical waves," *Phys. Rev. B* **89**, 134302 (2014).
- <sup>45</sup>F. Guinea, M. I. Katsnelson, and A. K. Geim, "Energy gaps and a zero-field quantum hall effect in graphene by strain engineering," *Nat. Phys.* **6**, 30–33 (2010).
- <sup>46</sup>K. K. Gomes, W. Mar, W. Ko, F. Guinea, and H. C. Manoharan, "Designer dirac fermions and topological phases in molecular graphene," *Nature* **483**, 306–310 (2012).
- <sup>47</sup>M. Hafezi, E. A. Demler, M. D. Lukin, and J. M. Taylor, "Robust optical delay lines with topological protection," *Nat. Phys.* **7**, 907 (2011).
- <sup>48</sup>M. Hafezi, S. Mittal, J. Fan, A. Migdall, and J. M. Taylor, "Imaging topological edge state in silicon photonics," *Nat. Photon.* **7**, 1001 (2013).
- <sup>49</sup>K. Fang, Z. Yu, and S. Fan, "Photonic Aharonov-Bohm effect based on dynamic modulation," *Phys. Rev. Lett.* **108**, 153901 (2012).
- <sup>50</sup>K. Fang, Z. Yu, and S. Fan, "Realizing effective magnetic field for photons by controlling the phase of dynamic modulation," *Nat. Photon.* **6**, 782 (2012).
- <sup>51</sup>M. C. Rechtsman, J. M. Zeuner, Y. Plotnik, Y. Lumer, D. Podolsky, F. Dreisow, S. Nolte, M. Segev, and A. Szameit, "Photonic floquet topological insulators," *Nature* **496**, 196 (2013).
- <sup>52</sup>L. D. Tzhang, K. Fang, P. Nussenzveig, S. Fan, and M. Lipson, "Non-reciprocal phase shift induced by an effective magnetic flux for light," *Nat. Photon.* **8**, 701 (2014).

- <sup>53</sup>F. Liu and J. Li, "Gauge field optics with anisotropic media," *Phys. Rev. Lett.* **114**, 103902 (2015).
- <sup>54</sup>M. C. Rechtsman, J. M. Zeuner, A. Tünnermann, S. Nolte, M. Segev, and A. Szameit, "Strain-induced pseudo magnetic field and photonic landau levels in dielectric structures," *Nat. Photon.* **7**, 153–158 (2013).
- <sup>55</sup>H. Schomerus and N. Y. Halpern, "Parity anomaly and Landau-level lasing in strained photonic honeycomb lattices," *Phys. Rev. Lett.* **110**, 013903 (2013).
- <sup>56</sup>H. Abbaszadeh, A. Soudov, J. Paulose, H. Schomerus, and V. Vitelli, "Sonic Landau levels and synthetic gauge fields in mechanical metamaterials," *Phys. Rev. Lett.* **119**, 195502 (2017).
- <sup>57</sup>X. Wen, C. Qiu, Y. Qi, L. Ye, M. Ke, F. Zhang, and Z. Liu, "Acoustic Landau quantization and quantum-Hall-like edge states," *Nat. Phys.* **15**, 352–356 (2019).
- <sup>58</sup>D. L. Miller, K. D. Kubista, G. M. Rutter, M. Ruan, W. A. de Heer, P. N. First, and J. A. Stroscio, "Observing the quantization of zero mass carriers in graphene," *Science* **324**, 924–927 (2009).
- <sup>59</sup>L.-H. Wu and X. Hu, "Scheme for achieving a topological photonic crystal by using dielectric material," *Phys. Rev. Lett.* **114**, 223901 (2015).
- <sup>60</sup>Y. Deng, H. Ge, Y. Tian, M. Lu, and Y. Jing, "Observation of zone folding induced acoustic topological insulators and the role of spin-mixing defects," *Phys. Rev. B* **96**, 184305 (2017).
- <sup>61</sup>C. He *et al.*, "Acoustic topological insulator and robust one-way sound transport," *Nat. Phys.* **12**, 1124–1129 (2016).
- <sup>62</sup>X. Zhang, M. Xiao, Y. Cheng, M. H. Lu, and J. Christensen, "Topological sound," *Commun. Phys.* **1**, 97 (2018).
- <sup>63</sup>G. Ma, M. Xiao, and C. T. Chan, "Topological phases in acoustic and mechanical systems," *Nat. Rev. Phys.* **1**, 281–294 (2019).
- <sup>64</sup>Y. Zhou, P. R. Bandaru, and D. F. Sievenpiper, "Quantum-spin-hall topological insulator in a spring-mass system," *New J. Phys.* **20**, 123011 (2018).
- <sup>65</sup>R. Fleury, D. Sounas, and A. Alu, "An invisible acoustic sensor based on parity-time symmetry," *Nat. Commun.* **6**, 1–7 (2015).
- <sup>66</sup>B.-I. Popa, Y. Zhai, and H.-S. Kwon, "Broadband sound barriers with bianisotropic metasurfaces," *Nat. Commun.* **9**, 5299 (2018).
- <sup>67</sup>C. Cho, X. Wen, N. Park, and J. Li, "Digitally virtualized atoms for acoustic metamaterials," *Nat. Commun.* **11**, 251 (2020).
- <sup>68</sup>J.-P. Xia, D. Jia, H.-X. Sun, S.-Q. Yuan, Y. Ge, Q.-R. Si, and X.-J. Liu, "Programmable coding acoustic topological insulator," *Adv. Mater.* **30**, 1805002 (2018).
- <sup>69</sup>Y. Chen, X. Li, G. Hu, M. R. Haberman, and G. Huang, "An active mechanical Willis meta-layer with asymmetric polarizabilities," *Nat. Commun.* **11**, 3681 (2020).
- <sup>70</sup>C. Caloz and Z.-L. Deck-Léger, "Spacetime metamaterials—Part I: General concepts," *IEEE Trans. Antennas Propag.* **68**, 1569 (2020).
- <sup>71</sup>X. Wen, X. Zhu, A. Fan, W. Y. Tam, J. Zhu, F. Lemoult, and J. Li, "Asymmetric frequency conversion with acoustic non-Hermitian space-time varying metamaterial," *arXiv:2011.01006* (2020).